Manipulation of Bacteria Using Three Dimensional Insulator Based Dielectrophoresis

by

William Allan Braff

B.S., Yale University (2005)

Submitted to the Department of Mechanical Engineering
in partial fulfillment of the requirements for the degree of

Master of Science in Mechanical Engineering

at the

MASSACHUSETTS INSTITUTE OF TECHNOLOGY

June 2011

Author .....
Department of Mechanical Engineering
May 6, 2011

Certified by .....
Cullen R. Buie
Assistant Professor
Thesis Supervisor

Accepted by .....
David E. Hardt
Graduate Officer, Department of Mechanical Engineering

Manipulation of Bacteria Using Three Dimensional Insulator Based Dielectrophoresis

by

William Allan Braff

Submitted to the Department of Mechanical Engineering
on May 6, 2011, in partial fulfillment of the
requirements for the degree of
Master of Science in Mechanical Engineering

Abstract

Insulator-based dielectrophoresis (iDEP) is a very promising technique for sorting microparticles based on their electrical properties. By using constrictions in a microchannel to generate large electric field gradients, the need for microfabricated electrode arrays is eliminated. In this work, three-dimensional insulator-based dielectrophoresis (3DiDEP) devices are fabricated using a novel micromachining technique. These devices are predicted and observed to exhibit higher trapping sensitivity than existing devices in the literature; this allows for efficient trapping of microparticles and bacteria at low applied fields with minimal thermal shock on the particles due to Joule heating effects. The dielectric properties of a range of bacteria, as well as polystyrene beads are examined. The impact of these results on the development of microbial fuel cells and portable low-cost clinical diagnostic tools is also discussed.

Thesis Supervisor: Cullen R. Buie
Title: Assistant Professor

Acknowledgments

I would first like to thank my advisor, Professor Cullen Buie, for his guidance and support throughout this work. I have learned a great deal from him over the last two years, and the opportunity he has afforded me by offering me a spot to study here at MIT has been invaluable.

I would also like to thank the other members of the Laboratory for Energy and Microsystems Innovation. Aron Blaesi, Zhifei Ge, Youngsoo Joung, Tim Palmer, and Alisha Schor are all excellent engineers, and have provided me with valuable advice and guidance on countless occasions.

I must pay particular thanks to Professor Korneel Rabaey for hosting me at the University of Queensland. His gracious hospitality not only made for a wonderful visit, but also made a large portion of the work presented here possible. I am equally indebted to Professor Peer Schenk, Holger Schumann, Natacha Juste-Poinapen, Serene Low, and Gary Morgan, also of the University of Queensland, for their experimental support throughout the visit. Thanks as well to Kelly Wrighton of the University of California, Berkeley for her help in teaching me anaerobic culture techniques, which would have been nearly impossible for me to learn on my own.

Lastly, this work would never have been possible without the patience and support of my wife, Georgiana. Her understanding and perspective have helped keep me on track throughout numerous highs and lows.

Contents

List of Figures

List of Tables

Chapter 1

Introduction

1.1 Dielectrophoresis

One of the most promising techniques for probing the dielectric properties of microparticles is dielectrophoresis (DEP), which is defined as the force due to a nonuniform electric field acting on the induced dipole of a particle suspended in a medium [38, 74, 10]. First observed by Pohl in 1951, DEP is a means to apply a force depending on the relative polarizability of a particle compared to that of the surrounding medium [73]. Traditional electrokinetic effects such as electrophoresis and electroosmosis involve the interaction of external electric fields with the thin layers of charge that form at the interfaces between different materials. Dielectrophoresis probes the dielectric properties of a material, independent of charge. For a spherical, homogenous particle with radius a (domain 2) in a medium of permittivity ε_m with an applied DC electric field (domain 1), the dielectrophoretic force on the particle can be expressed as

$$\overline{F}_{\mathrm{DEP}} = 2\pi\varepsilon_1 a^3 \kappa_{CM} \nabla E_0^2. \tag{1.1}$$

In this case, the Clausius-Mossotti factor κ_{CM} can be written in terms of the complex permittivities of the particle and media:

$$\kappa_{CM} = \frac{\varepsilon_2^* - \varepsilon_1^*}{\varepsilon_2^* + 2\varepsilon_1^*}. \tag{1.2}$$

A fuller understanding of DEP will be introduced in chapter 2, but this simple case is sufficient to highlight several key properties of the effect. Perhaps most importantly, because force is proportional to the gradient of the electric field intensity, polarity of the system is unimportant, so AC fields work just as well as DC fields. Additionally, because the Clausius-Mossotti factor κ_{CM} is a function of the dielectric properties of the particle and medium, the strength and sign of the force is determined by dielectric properties, which allows for an additional degree of freedom in selecting for particles with a desirable set of properties.

Initial work to observe and identify DEP generally involved needles, wires, and flat surfaces to generate inhomogenous electric fields [73, 74]. However, the forces generated in these studies were small, and the work received relatively little attention. However, the application of microfabrication techniques developed by the semiconductor industry in the nineteen eighties to fabricate arrays of microelectrodes allowed for the generation of larger field intensity gradients with lower applied fields [76, 61, 27]. This capability made it possible to apply dielectrophoresis to biological particles without damaging them. Studies were conducted that used DEP to trap and sort biological particles including plant, algal, mammalian, bacterial, and yeast cells as well as viruses and DNA [40, 28, 11, 60, 36, 64, 99].

Insulator-based dielectrophoresis (iDEP), an alternative to traditional microelectrode based systems, employs insulating structures such as an array of posts or other structures to create gradients in an otherwise uniform electric field generated by macroscopic electrodes placed at either end of a microfluidic channel [22]. In this type of system, bulk fluid flow is commonly generated by electroosmotic flow due to an applied DC electric field. This eliminates the need for an external pump, and the balance of electroosmotic flow, electrophoresis, and dielectrophoresis acting on particles can be tuned depending on the field strength to induce focusing as well as trapping effects. Such systems have been applied to a wide variety of applications, including live-dead sorting [44, 45], cell concentration [19], as well as to enhance the kinetics of DNA hybridization [95]. DC-biased AC electric fields have also been investigated as a way to increase the flexibility of iDEP by varying the relative magnitudes

of the DC and AC components of the field, as well as by introducing novel geometries to sort particles spatially [105, 33]. However, the large DC voltages typically required to create sufficiently large DEP forces can lead to Joule heating and electrothermal flows, both of which can disrupt successful trapping [32].

1.2 Extracellular Electron Transfer

Under normal circumstances, microbes derive energy from a substrate by oxidizing it, and then transferring the electrons to an available acceptor such as oxygen, nitrate, or fumarate. The energy released in this process is harnessed by the microbe for use in various cellular functions. In the absence of any available electron acceptors, under certain circumstances, the electrons can be transferred extracellularly to an electrode, which serves as the anode. As long as the anode is electrically and ionically connected to a cathode, where an electron acceptor is made available, the reduction half-reaction can be performed there. If an external load is inserted into the electrical path between anode and cathode, energy can be harvested from this process in the form of useful work.

The motivation for identifying bacteria with the ability to respire using an electrochemical anode came from the early discovery of bacteria present in anaerobic freshwater sediments that were able to metabolize a number of organic substrates using amorphous ferric iron (Fe[III]) [54]. Since most cellular respiration requires the presence of a soluble electron acceptor, the study of dissimilatory metal reducing bacteria that can respire on insoluble acceptors attracted significant attention. Further work isolated a number of bacteria with the ability for extracellular electron transfer to ferric iron as a terminal electron receptor [55]. Similar capabilities were also demonstrated with chromium, cobalt, manganese, technetium, and uranium [65, 57, 56, 102, 29, 85, 66, 58, 48]. The ability to reduce elemental sulfur and humic substances was also shown for certain species.[51, 84, 53, 87] Concurrent observations that the iron-reducing bacterium *Shewanella putrefaciens* was able to use an electrode rather than a metal oxide as an electron acceptor prompted the first examples

of mediator-less fuel cells [41, 42, 43]. Although these were by no means the first microbial fuel cells, they represented a major step forward from previous systems in that they did not require the addition of external mediators, which are often toxic, to shuttle electrons between the bacteria and the electrode.

Further study of this class of bacteria gave rise to general classes of bacteria capable of extracellular electron transfer. One class, which includes the genus *Shewanella*, transfers electrons by producing flavins that serve as its own mediators [13, 98]. The second, which includes the genus *Geobacter*, cannot produce mediators, and instead relies on structures in the surface of its outer membrane to transfer electrons directly [68, 6, 7]. *Geobacter sulfurreducens* strain PCA in particular has attracted considerable attention, in part because of the high power output it has been able to achieve in microbial fuel cells [69].

G. sulfurreducens strain PCA relies on proteins in its cellular membrane, in particular c-type cytochromes, in order to transfer electrons. These cytochromes have also shown to serve as temporary electron sinks, in order to maintain cell motility while moving between different electron acceptor sites [24]. Deletion mutants of *G. sulfurreducens* in which genes for the c-type cytochromes OmcS and OmcE were removed were shown to be unable to reduce insoluble Fe(III) [62]. However, later studies showed that the OmcS and OmcE deletion mutants were able to respire on an electrode, but that OmcZ and OmcB deletion mutants missing were not [82]. At the same time, scanning tunneling electron microscopy studies showed that pili also present in the outer membrane were electrically conductive, effectively serving as 'nanowires' to promote electron transfer [80]. These nanowires were not required for electron transfer when the bacteria were in direct contact with the electrode [35], but studies showed that their presence allowed bacteria to form thicker biofilms, with an increase in current production proportional to the biomass present, suggesting that bacteria that were as far as 50 μm away from the electrode were able to transfer electrons [81]. Microarray studies of gene transcript levels confirmed that bacteria cultured in a microbial fuel cell exhibited increased gene transcript levels for genes associated with the formation of pili, OmcB, and OmcZ compared with bacteria cultured on a

soluble electron acceptor such as fumarate [67].

The discovery that *G. sulfurreducens* could transfer electrons to an electrode via an electrically conductive matrix of bacterial nanowires and bacteria rather than through direct contact represented a major step forward in understanding why it tended to outperform other bacteria capable of direct extracellular electron transfer in bioelectrochemical cells. However, the dielectric properties of the conductive matrix are still largely unknown, and the need for tools to characterize these properties remains unmet.

1.3 Microbial Fuel Cells

The need for renewable, low-cost sources of electricity is one of the major challenges facing society today. In particular, developing countries with limited infrastructure and economic resources need a means to provide power to remote populations. Microbial fuel cells are an emerging technology with a number of advantages over competing technology. Microbial fuel cells can operate continuously, avoiding the intermittency problems of photovoltaic and wind turbine energy sources [3], and since they can operate on widely available organic materials such as wastewater, they do not require the significant capital investment of traditional fuel cell systems in order to produce and distribute fuels, either in liquid or gas form [70]. An additional benefit of these systems is that as they oxidize substrates present in the wastewater, they greatly reduce its total oxygen demand, thereby simplifying further treatment costs [26]. These attributes position microbial fuel cells to play a major role in energy production for regions of the world with limited energy distribution networks.

Microbial fuel cells are similar to traditional fuel cells in that fuel and oxidant are supplied to two electrodes, the anode and cathode, respectively. An electrolyte separates the electrodes, and provides for ionic conduction between them. For an example system operating on glucose, the net reactions in the systems could be written as:

$$\begin{aligned} \text{anode: } C_6H_{12}O_6 + 6H_2O &\rightarrow 6CO_2 + 24H^+ + 24e^- \\ \text{cathode: } 6O_2 + 24H^+ + 24e^- &\rightarrow 12H_2O \\ \text{net: } C_6H_{12}O_6 + 6O_2 &\rightarrow 6H_2O \end{aligned} \tag{1.3}$$

Under standard conditions, the anode and cathode half reactions have equilibrium potentials of 0.01 V and 1.23 V respectively [90]. The potential difference between the two electrodes drives current in the circuit, and electricity is produced.

However, rather than using an electrocatalyst such as platinum to drive the anode half reaction as in a traditional fuel cell, a microbial fuel cell relies on the ability of certain types of microorganisms to oxidize an organic substrate such as glucose, acetate, or lactate, and then transfer electrons to the anode. The ability to produce electricity using microorganisms has been documented as far back as the early 20th century [52, 90, 75]. However, the last ten years has seen renewed attention in the field, accompanied by a million fold increase in the power density generated by microbial fuel cells [49]. Proposed systems have varied in reactor volume from microliters [78, 14] to several liters [104], and several pilot scale reactors have also been installed in industrial environments [50].

A major portion of the the improvements in cell performance to date have been the result of innovations in system design. In particular, the implementation of single chamber, air cathode systems drastically improved performance [47, 46]. Compared to previous systems that typically typically employed a two chamber design [6, 16], these new cell designs were no longer limited by internal resistance kinetic losses at the cathode, resulting in a thousand-fold improvement in power density. Other system-based developments include incorporating membrane electrode assembly technology from the traditional fuel cell industry to further reduce internal resistance [12], as well as nano liquids and carbon nanotubes in order to aid electron transfer processes at the anode [88]. As present, the highest power microbial fuel cells are able to achieve 3 W/m^2 using a isolated culture of *Shewanella oneidensis* DSP10 [83], and as much as

4.3 W/m^2 using a mixed culture [79]. In a separate study, a system with asymmetrical anode and cathode reached a power density of 6.9 W/m^2, normalized to the anode [25].

Although the gains recorded in the past ten years are remarkable, there is evidence that system design improvements have more or less reached their limits using existing bacterial strains. In one study, authors predicted that even if system resistance could be eliminated, power output would peak at 19.4 W/m^2 [25]. In another, basic mass transport arguments were used to estimate a peak power of 17 W/m^2 [49]. Although these power levels represent significant progress over earlier work, they significantly limit the commercial potential of this technology. In order move beyond these limitations, improvements to the microbes that perform the fuel oxidation are required.

1.4 Organization

In this work, microfluidic devices were designed and fabricated in order to study the dielectric properties of bacteria. These devices employ insulator-based dielectrophoresis to trap and select for bacteria based on their outer membrane properties. A novel fabrication technique was used in order to achieve high sensitivity, which allows for trapping of bacteria at much lower applied voltages than in previous works. The device was then used to examine the dielectric properties of several different types of bacteria. The work is organized as follows.

Chapter 2 discusses the physics of DEP, and how it can be harnessed in an iDEP device to examine the dielectric properties of microparticles. Chapter 3 discusses the design and fabrication of two and three dimensional microfluidic devices that employ DEP to trap microparticles. Chapter 4 examines the predicted behavior of the devices using analytic and numerical models to describe the physics of the system. Chapter 5 applies the devices of the previous chapter to bacteria and microparticles, and chapter 6 provides conclusions and discusses potential future work.

Chapter 2

The Physics of Dielectrophoresis

2.1 Introduction

Over the past ten years, roughly 2000 papers have been published on dielectrophoresis (DEP) [72]. As the theory and techniques surrounding it have matured, more and more work has been published looking at potential lab-on-a-chip applications. This is in large part due to the unique properties of DEP, which we will now examine in depth. Because DEP is a nonlinear electrokinetic effect that does not depend on the charge of the particle or the polarity of the applied field, first order electrostatic intuition is insufficient to predict its effects. It is therefore instructive to formally derive its behavior starting from electrostatics. The general results discussed here will be used later to understand the more specific modeling results presented in chapter 4.

2.2 Multipole Expansion of Force on a Dielectric Particle

First, consider a polarizable sphere of radius r centered at $\mathbf{r}_0$ in a nonuniform field $\mathbf{E}$. The derivation presented here will roughly follow that of Bruus, but there are several other sources in the literature, originating back to Pohl [38, 73, 74, 10]. When a particle or region with local charge density $\rho(\mathbf{r})$ is placed in the electric field $\mathbf{E}$,

elementary electrostatics dictates that it will experience a coulombic force. The force acting on the particle can be written as

$$F_i = \int_V \rho(\mathbf{r} - \mathbf{r}_0) E_i(\mathbf{r} - \mathbf{r}_0) dV \tag{2.1}$$

Expand the electric field as a power series to second order:

$$E_i(\mathbf{r} - \mathbf{r}_0) \approx E_i(\mathbf{r}_0) + (\mathbf{r} \cdot \nabla) E_i|_{\mathbf{r}=\mathbf{r}_0} + \frac{1}{2}\mathbf{r} \cdot (\mathbf{r} \cdot \nabla(\nabla E_i))|_{\mathbf{r}=\mathbf{r}_0}, \tag{2.2}$$

so the force can be written:

$$\begin{aligned} F_i &\approx \int_V \rho(\mathbf{r} - \mathbf{r}_0) dV E_i(\mathbf{r}_0) \\ &+ \left(\int_V \rho(\mathbf{r} - \mathbf{r}_0) \mathbf{r} dV \cdot \nabla \right) E_i|_{\mathbf{r}=\mathbf{r}_0} \\ &+ \frac{1}{2} \left(\left(\int_V \rho(\mathbf{r} - \mathbf{r}_0) \mathbf{r}\mathbf{r} dV \cdot \nabla \right) \cdot \nabla \right) E_i|_{\mathbf{r}=\mathbf{r}_0}. \end{aligned} \tag{2.3}$$

This is simply a multipole expansion of the force on the particle, where the integral terms represent the monopole, dipole, and quadrupole contributions, respectively. Define the net charge, dipole moment, and quadrupole tensor as:

$$\begin{aligned} q &= \int_V \rho(\mathbf{r} - \mathbf{r}_0) dV \\ \mathbf{m} &= \int_V \rho(\mathbf{r} - \mathbf{r}_0) \mathbf{r} dV \\ \mathbf{Q} &= \int_V \rho(\mathbf{r} - \mathbf{r}_0) \mathbf{r}\mathbf{r} dV. \end{aligned}$$

For a neutral particle, $q = 0$, and the monopole term is exactly zero. Assuming the length scale l over which the electric field changes is much larger than r, a quick scaling analysis shows that $|\mathbf{Q}| \ll |\mathbf{m}|$, so second and higher order terms can be neglected. Under these conditions, the force on a polarizable but neutral particle can be expressed as:

$$\mathbf{F}_{DEP} = (\mathbf{m} \cdot \nabla)\mathbf{E}. \tag{2.4}$$

The above assumptions are valid for all of the situations commonly encountered in microfluidic DEP systems, so equation 2.4 is commonly treated as the canonical equation for DEP.

2.3 Key Elements of DEP

It can be shown that the dipole moment of a particle can be written in closed form as [64, 39]

$$\mathbf{m} = 3\varepsilon_m V \mathrm{Re}\{\kappa_{CM}\}\mathbf{E}. \tag{2.5}$$

The general expression for a force due to DEP is then:

$$\mathbf{F}_{DEP} = \frac{3}{2}\varepsilon_m V \mathrm{Re}\{\kappa_{CM}\}\nabla E^2. \tag{2.6}$$

Here V is the volume of the particle, ε_m is the dielectric constant of the surrounding media, and κ_{CM} is the complex Clausius-Mossotti factor. Many microscopic biological particles such as bacteria and algae can be treated either as spheres or prolate ellipsoids with weakly conductive outer shells. In this approximation, they can be described in terms of their semi-axes a_1, a_2, and a_3 as defined in figure 2-1. For the case where major semi-axis $a_1 > a_2, a_3$ is aligned with the applied field, the Clausius-Mossotti factor is [39]:

$$\begin{aligned} \kappa_{CM} &= \frac{1}{3}\frac{\varepsilon_p^* - \varepsilon_m^*}{(\varepsilon_p^* - \varepsilon_m^*)A + \varepsilon_m^*} \\ \varepsilon_j^* &= \varepsilon_j - i\frac{\sigma_j}{\omega} \\ A &= \frac{3V}{8\pi}\int_0^\infty \frac{d\xi}{(a_1^2+\xi)R} \\ R &= \left[(a_1^2+\xi)(a_2^2+\xi)(a_3^2+\xi)\right]^{1/2}. \end{aligned} \tag{2.7}$$

In these expressions, ε_p^* and ε_m^* are the complex dielectric constants of the particle and media respectively. They are functions of the dielectric constants ε_j, as well

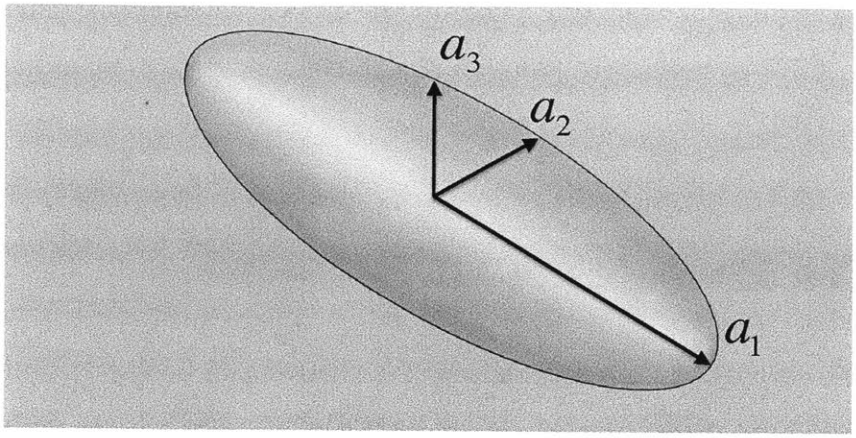

Figure 2-1: An ellipsoid can be defined in terms of its semi-axes, a_1, a_2, and a_3

as the particle conductivity σ_j and applied frequency ω. Inhomogeneous multi-shell models can also be treated in this framework by iteratively calculating an effective ε_p^* for composite particles, and then applying an additional shell outside [39]. For the general case of an ellipsoid, the depolarizing factor A can be nontrivial to calculate, but for two limiting cases: that of a spherical particle ($a_1 = a_2 = a_3$) and that of a skinny prolate ellipsoid or rod ($a_1 \gg a_2, a_3$), the Clausius-Mossotti factor takes on simple forms:

$$\kappa_{CM}^{sph} = \frac{\varepsilon_p^* - \varepsilon_m^*}{2\varepsilon_m^* + \varepsilon_p^*} \tag{2.8}$$

$$\kappa_{CM}^{rod} = \frac{\varepsilon_p^* - \varepsilon_m^*}{3\varepsilon_m^*}. \tag{2.9}$$

For operating frequencies below roughly 100 kHz, it is trivial to show that the imaginary terms dominate over the real ones in the complex permittivities, so that the Clausius-Mossotti factors become functions only of particle and media conductivity. For insulator-based dielectrophoresis (iDEP), technical limitations of high voltage power supplies typically keep the applied frequencies below 10 kHz, so the constraint is always well satisfied. It is then straightforward to work out the force due to DEP on homogeneous spheres and rods:

$$\mathbf{F}_{sph} = 2\varepsilon_m \pi a_1^3 \frac{\sigma_p - \sigma_m}{2\sigma_m + \sigma_p} \nabla E^2 \tag{2.10}$$

$$\mathbf{F}_{rod} = \frac{2}{3}\varepsilon_m \pi a_1 a_2^2 \frac{\sigma_p - \sigma_m}{\sigma_m} \nabla E^2. \tag{2.11}$$

Since this work is directed towards iDEP of either spherical microparticles or rod-shaped bacteria, these two expressions are adequate to describe the forces due to DEP observed in these devices.

Although the Clausius-Mossotti factors are very similar for the spherical and rod-shaped cases, they can take on slightly different functional forms. This is particularly true in the case of positive DEP, in which case the Clausius-Mossotti factor for rods has a positive asymptote, whereas for spheres it is bounded at one. This effect is shown in figure 2-2. For the majority of situations, the two cases follow very similar trends, and the same general intuition applies.

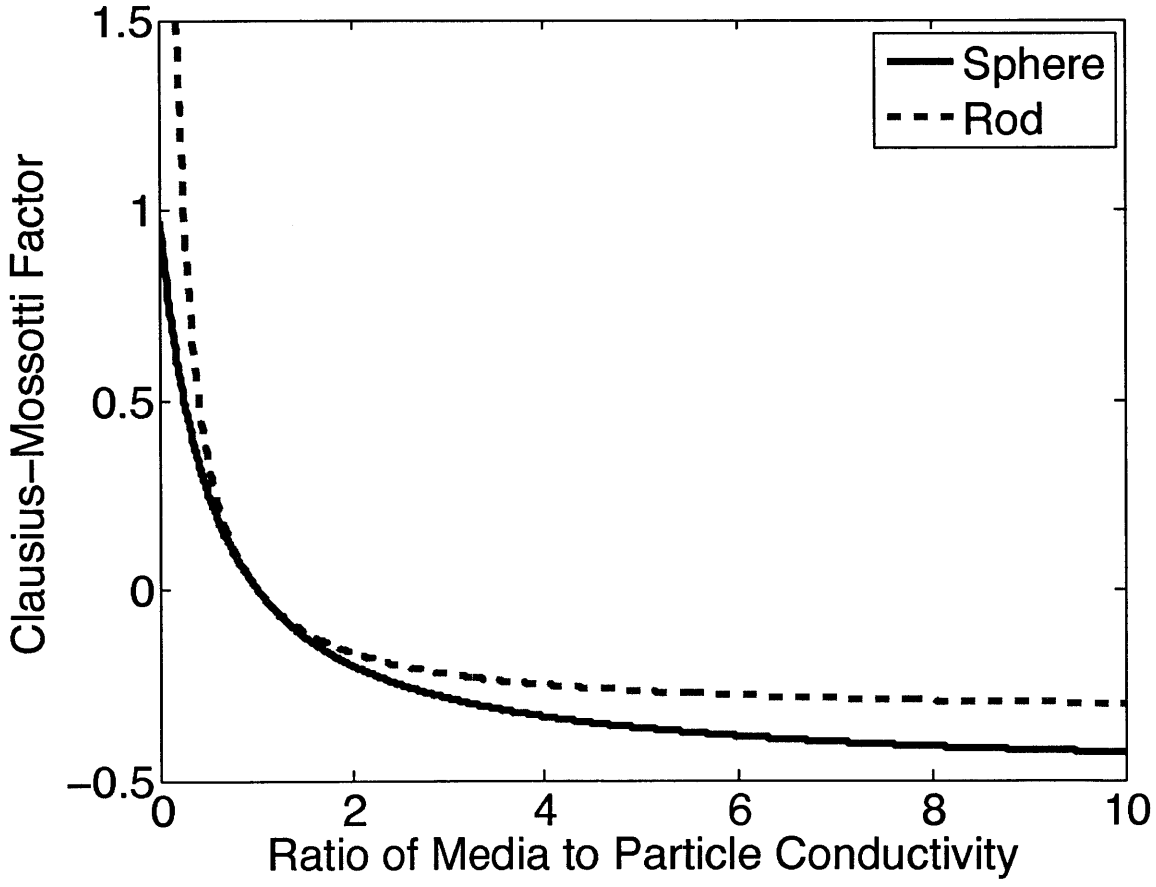

Figure 2-2: Clausius-Mossotti factor in a DC field for rod shaped and spherical particles as a function of particle conductivity

2.4 Physical Description of DEP

For a more intuitive physical understanding of this effect, it is instructive to consider the simple case of a homogeneous sphere suspended in polarizable media in a nonuniform electric field, as shown in figure 2-3. In this system, net dipoles form within the particle nearest the positive and negative electrodes. At the same time, screening dipoles form in the media just outside of the particle. If the media is more polarizable than the particle, than the screening dipoles will be stronger than the particle dipoles, and the particle will experience a net force away from the region of highest field intensity. If the polarity of the electrodes is reversed, the resultant force is unchanged. Likewise, if the particle is more polarizable than the media, the screening dipoles will be unable to shield the induced dipole inside the particle, and it will be attracted to the region of highest field intensity. This physical explanation describes the $F \propto \nabla E^2$ behavior that is unique to DEP.

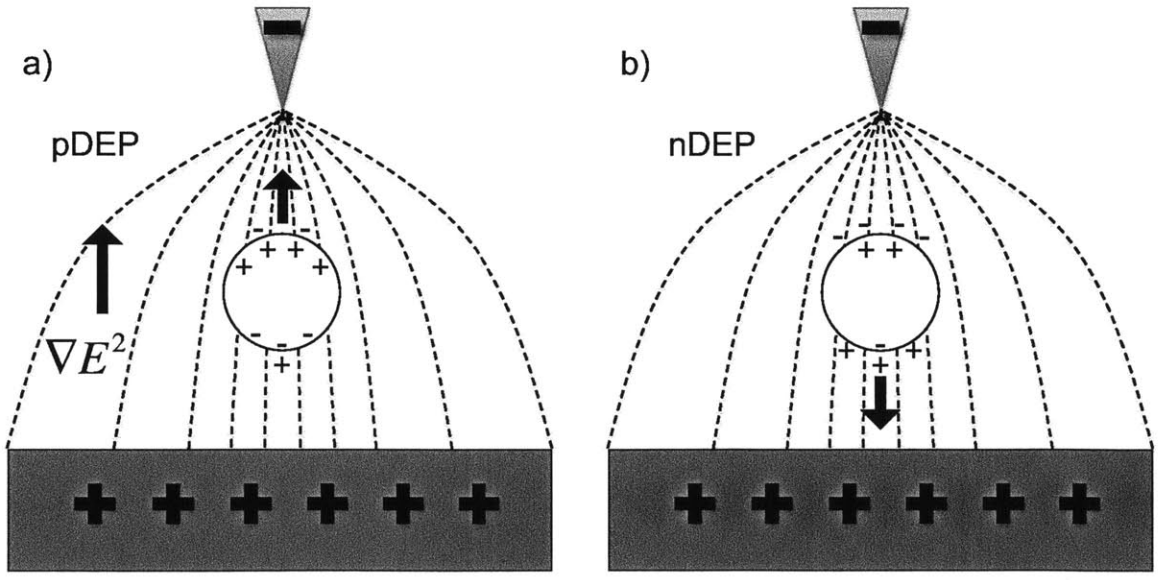

Figure 2-3: Schematic of (a) positive and (b) negative dielectrophoresis

In order to understand the motivation for the designs described in chapter 3, it is useful to understand the basic mechanics of DEP trapping. In iDEP devices such as the ones described in this work, a low frequency electric field with a DC bias is applied across the channel. The electroosmotic mobility of the fluid-channel interface drives

bulk fluid flow, and if the particles have a non-zero zeta potential, electrophoresis will also contribute to particle motion. Near the constriction, continuity arguments stipulate that the current density magnitude, and therefore the electric field intensity, reaches a maximum. Particles such as polystyrene beads, which can be treated as perfect insulators in aqueous buffers, will experience negative DEP as they approach the constriction. This force will repel the particles as they approach the constriction, and if it is sufficiently strong, will stop the particles from passing through the constriction. In the case of certain types of bacteria in low conductivity media, the relatively conductive cell membranes can be more polarizable than the media. When this occurs, the cells will experience positive DEP, which will drag them back towards the constriction after they have passed through. Again, when the DEP force is sufficiently strong, the particles will stopped.

A quick inspection of equations 2.10 and 2.11 reveals that there are three main factors in determining DEP force. The first is the volume of the particles; larger particles experience stronger forces than smaller once. The second is the Clausius-Mossotti factor, which is a function of the media and particle conductivity. It is this parameter that allows iDEP devices to select for particles within a population that have unique dielectric properties. For example, a bacterium with a high concentration of polarizable extracellular polysaccharides would experience a measurably different DEP force than one with a lower concentration under otherwise identical conditions. The third factor is the gradient of the electric field intensity. Size and Clausius-Mossotti factor of the particles being studied are beyond the control of the experimenter, but the gradient of the electric field intensity can be increased to improve the device's sensitivity, or variation in trapping performance for a given change in dielectric properties. There are two ways of increasing this: increasing the applied field, and increasing the field intensity gradient within the device. The three-dimensional insulator-based dielectrophoresis device presented in chapter 3 employs a large constriction ratio in order to maximize the field intensity gradient, thereby increasing the DEP forces that it applies on the particles under test. A more detailed analysis of device sensitivity is described in chapter 4.

Chapter 3

Design, and Fabrication of Microfluidic Devices

3.1 Introduction

Insulator-based dielectrophoresis (iDEP) relies upon a large gradient in electric field intensity in order to create forces large enough to overcome electroosmotic flow. Many geometries have previously been investigated, including arrays of square and circular pillars at various angles, as well as single constrictions [44, 22]. One clear conclusion of these papers, which will be discussed in more detail in chapter 4, is that the constriction ratio between the cross-sectional area of the channel and the cross-sectional area of the constriction is critical in order to efficiently trap small particles such as bacteria.

However, there are some practical constraints on how large the constriction ratio can be, since the constriction area cannot be arbitrarily small, and the channel area cannot be arbitrarily large. If the constriction area is not sufficiently larger than the particle size, steric interactions will block the channel resulting in trapping regardless of particle dielectric properties. Likewise, the width of the channel is often limited by the fabrication process, since in many cases very wide channels are prone to collapse.

One way to overcome these technical limitations is to constrict the channel in more than one dimension. By making the constriction not only narrower but shallower than

the rest of the channel, the constriction ratio of the device can be increased drastically. However, such a strategy requires fabrication techniques capable of making three-dimensional geometries.

The most common technique currently used for fabricating microfluidic devices is soft lithography, in which polydimethylsiloxane (PDMS) is poured on top of a patterned mold constructed using photolithography, and then the PDMS is bonded to a glass wafer using oxygen plasma treatment [103]. Although this procedure has many advantages, the time consuming multistep exposure procedures necessary to produce complex three-dimensional geometries, which would be necessary to create appropriate molds, are impractical for complicated constriction patterns. Furthermore, the surface charge characteristics of PDMS tend to exhibit transient effects that would result in unstable device performance for a system that relies on channel surface charge in order to drive flow.

Devices fabricated from borosilicate wafers have also been used for microfluidic devices. Although these devices exhibit more controllable electrokinetic phenomena than PDMS, and can be fabricated with high precision, they require multiple clean-room procedures with hazardous chemicals and are labor intensive to produce. Although much of the work described here could have been performed using borosilicate devices, the end goal of this work was to provide an inexpensive, easily scalable device for high-throughput characterization of bacteria. Clearly, a new fabrication procedure was needed.

In this chapter, the development of a novel fabrication process for micromachining microfluidic chips out of poly(methyl methacrylate) (PMMA) is described. This process allows for fully three dimensional features to be machine into the channel without multiple lithography steps. It also provides rapid development cycles and the potential for easier scale up to volume production, the importance of which will be discussed in chapter 6.

3.2 Channel Design

By using conventional three-axis milling processes to fabricate the channel, it was possible to easily vary the channel depth independently of constriction depth. A microfluidic device was designed with a 500 μm wide and 500 μm deep channel, and a 50 μm wide and 50 μm deep constriction. This created a constriction ratio of 100:1. The constriction size was chosen in order to maximize constriction ratio while minimizing steric obstructions for particles 1 - 10 μm in diameter. The precise benefits of this device over lower constriction ratio devices will be investigated in more detail in chapter 4, but most generally, the higher the constriction ratio, the greater the gradient in electric field intensity, which increases the dielectrophoretic force around the constriction as described by equation 1.1. A schematic of the three-dimensional insulator-based dielectrophoresis (3DiDEP) channel is shown in figure 3-1. A two-dimensional insulator-based dielectrophoresis (2DiDEP) channel was also designed for comparison. It was identical in design to the 3DiDEP device, except that the channel and constriction both had a depth of 50 μm, resulting in a constriction ratio of 10:1. This primary purpose of this device was to provide a reference design similar to those extant in literature [32]. A schematic of the 2DiDEP device is shown in figure 3-2.

Material selection was also very important. Optical transparency, minimal autofluorescence, good machinability, and well characterized electrokinetic properties were all important parameters. PMMA met all of these requirements, and was chosen for this work. Its low cost and wide availability were also significant when future scale up was considered. One and a half mm PMMA sheet was supplied by McMaster-Carr, of Robbinsville, NJ. Chips were fabricated from 25 $\times$ 55 mm pieces of PMMA that were made by scoring and breaking using a razor blade and a straight edge. In order to reduce fabrication time, seven channels were machined into each chip.

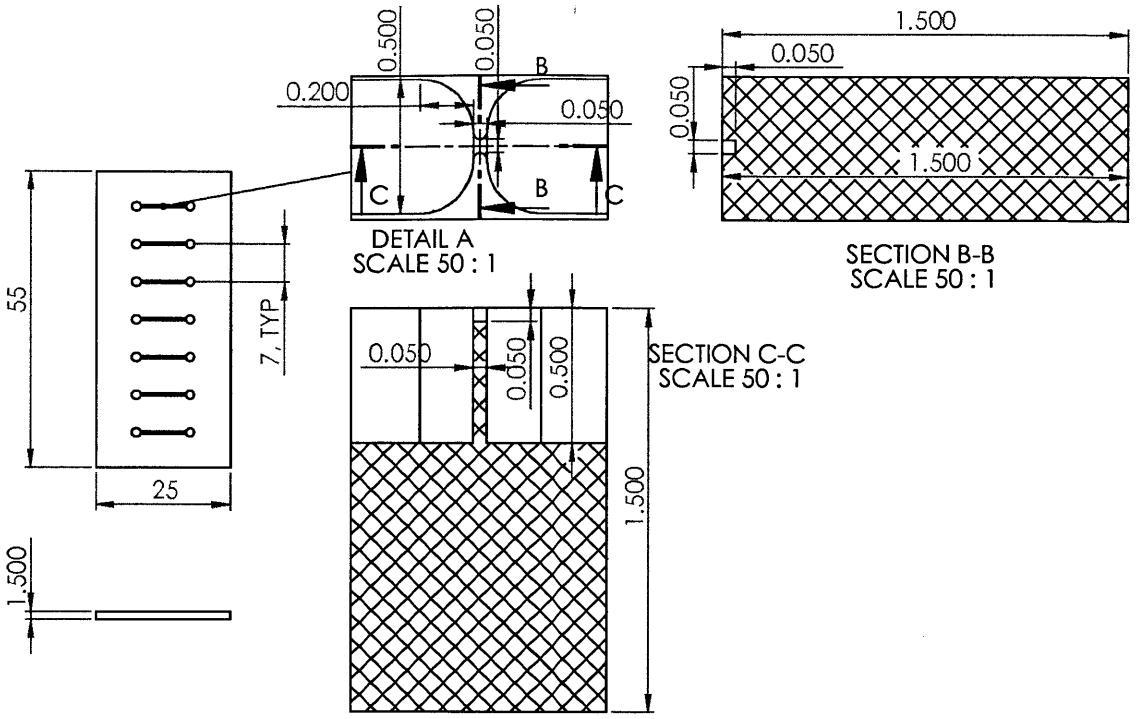

Figure 3-1: Design for the three-dimensional insulator-based dielectrophoresis (3DiDEP) microfluidic chip

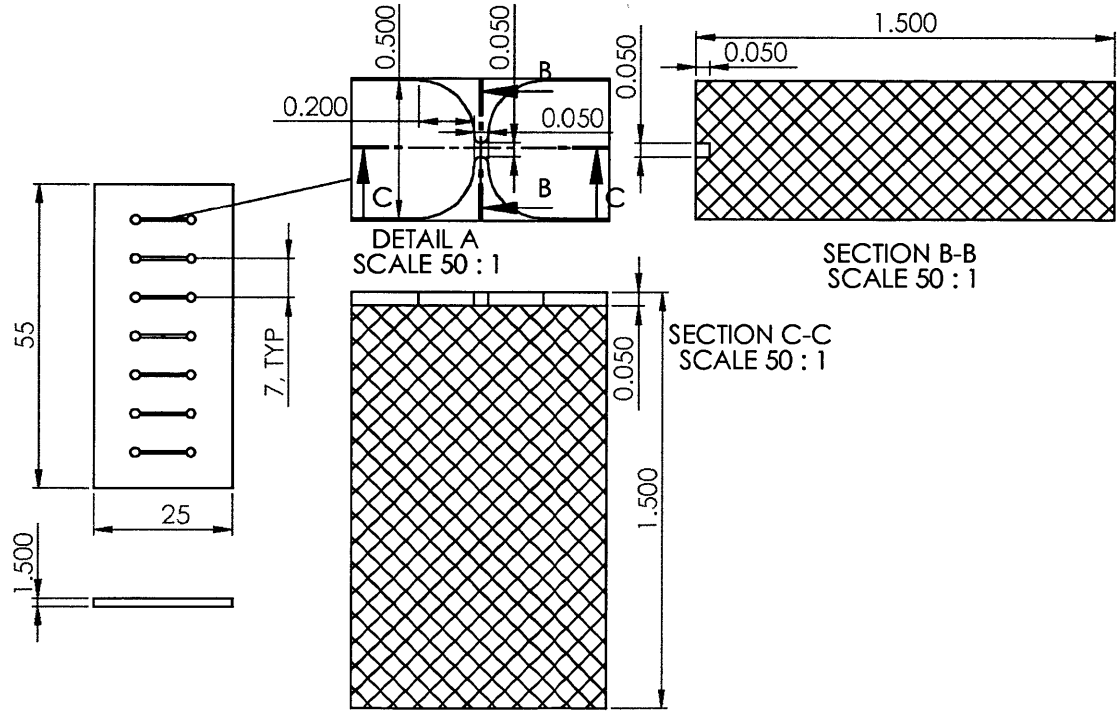

Figure 3-2: Design for two-dimensional insulator-based dielectrophoresis (2DiDEP) microfluidic chip

3.3 Micromachining

Although soft lithography techniques have been around for over a decade, efforts to apply them them at a large scale have been unsuccessful. In particular, the need for batch procedures in a clean room has severely inhibited scale up efforts. By comparison, CNC machining, initially developed at MIT in the 1950s, has played a major role in the production of a wide variety of products [101]. Although initial CNC work was directed towards the fabrication of large parts such as airfoils, more modern machines are able to repeatably generate patterns with sub micron repeatability. In this work, a 3-axis horizontal micro milling machine, the Microlution 363-S, was used to machine channels and constrictions. The mill used G Code, a common CNC control language, to define the tool path [91]. In order the generate G-code from the designs shown in figures 3-2 and 3-1, Mastercam, a CAD/CAM commercial software package was used to define precise toolpaths. Sufficiently small features were resolved using 50 μm, 380 μm, and 1.59 mm endmills purchased from Performance Micro Tool of Janesville, WI. Standard length, solid carbide, 2 flute tools were chosen for versatility. A photograph of all three tools and micrographs of the 50 μm and 381 μm tools are shown in figure 3-3. The exact G code used to fabricate the 3DiDEP device is included in appendix A. Machining time for this code including manual tool changes was approximately fifteen minutes.

One of the most significant challenges of micron-scale machining was defining workpiece offsets. Although the point to point precision of the mill is better than 1 μm and the tools themselves are made to very tight tolerances, the mill needs a starting point, or zero, in order to accurately machine parts. In traditional milling processes, the workpiece surface is defined simply by bringing the stationary tool into contact with the workpiece, and defining that position as zero. Unfortunately, very small tools will invariably break when this approach is employed. In order to address this problem, a laser touch-off procedure is built into the micro mill. In this procedure, the workpiece surface height is defined by bringing a 'blank', or steel cylinder with no cutting surfaces into contact with the workpiece. The tip of the blank is measured

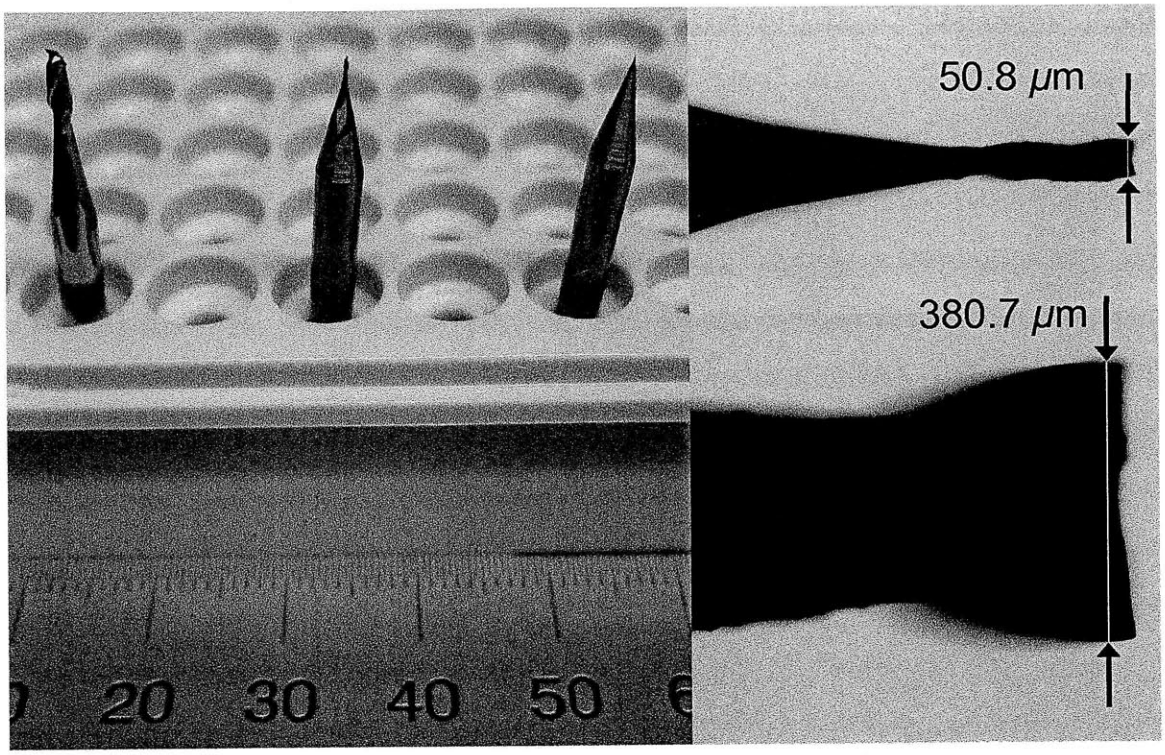

Figure 3-3: Photograph and micrographs of standard length, two flute micro endmills used for device fabrication

using a laser, and then the operator replaces the blank with the cutting tool. Its length is again measured with a laser, and the difference in length between the tool and the blank is stored by the mill as the tool offset. A schematic of this process is shown in figure 3-4.

An additional complication associated with workpiece offsets arose due to the mounting technique used. Initially, 100 μm two-sided adhesive tape was used to mount the PMMA to the milling pallet. However, the compressibility of the tape produced some hysteresis and uncertainty in the offset measurements. This effect was eliminated by replacing the soft adhesive tape with Crystalbond 555, a temporary mounting adhesive obtained from SPI Supplies, of West Chester, PA. This adhesive melts above 50°C, but remains solid at ambient temperatures so that the PMMA could be easily and securely mounted to the pallet. This mounting technique was observed to effectively eliminate offset hysteresis during the machining process. In addition, a facing procedure was incorporated into the G code to eliminate any offset

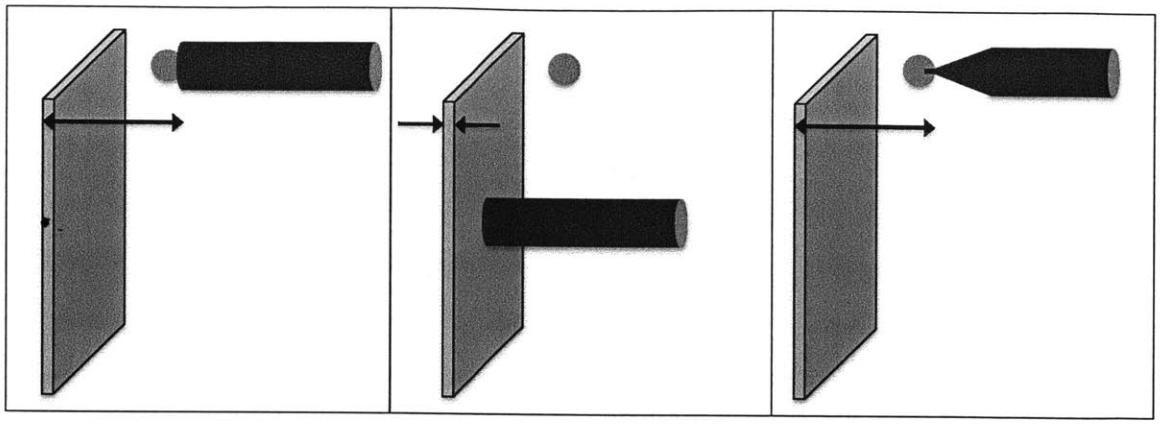

Figure 3-4: The mill uses a blank to determine the workpiece surface, and then uses a laser to determine the difference in length between the blank and the cutting tool

errors that might otherwise occur due to imperfect mounting of the PMMA. Such errors would result in features at one end of the device being a different depth than identical features at the other end.

Although the laser tool measurement process was very successful with tools of diameter greater than roughly 100 μm, the cutting diameter of smaller tools was insufficient to adequately occlude the laser beam. As a result, the tool measurement lengths for the 50 μm tool were incorrect. Calibration devices were fabricated and then cut in halt to obtain channel cross-sections. The discrepancy between observed tool length and measured tool length were characterized, as shown in figure 3-5. An offset of 35 μm was observed and incorporated into the G code manually.

3.4 Device Assembly

Once the chips were machined, they were removed from the pallet using a hotplate to melt the adhesive. Any excess adhesive was removed carefully with a lint-free cleaning wipe. The chips were then suspended in 65°C water agitated with a magnetic stirrer for ten minutes in order to remove any residual adhesive. After the adhesive was removed and the chip was inspected under a microscope to insure that it was free of defects, the chip as well as a blank piece of PMMA of the same dimensions were rinsed successively with acetone, methanol, isopropanol, and deionized water in order

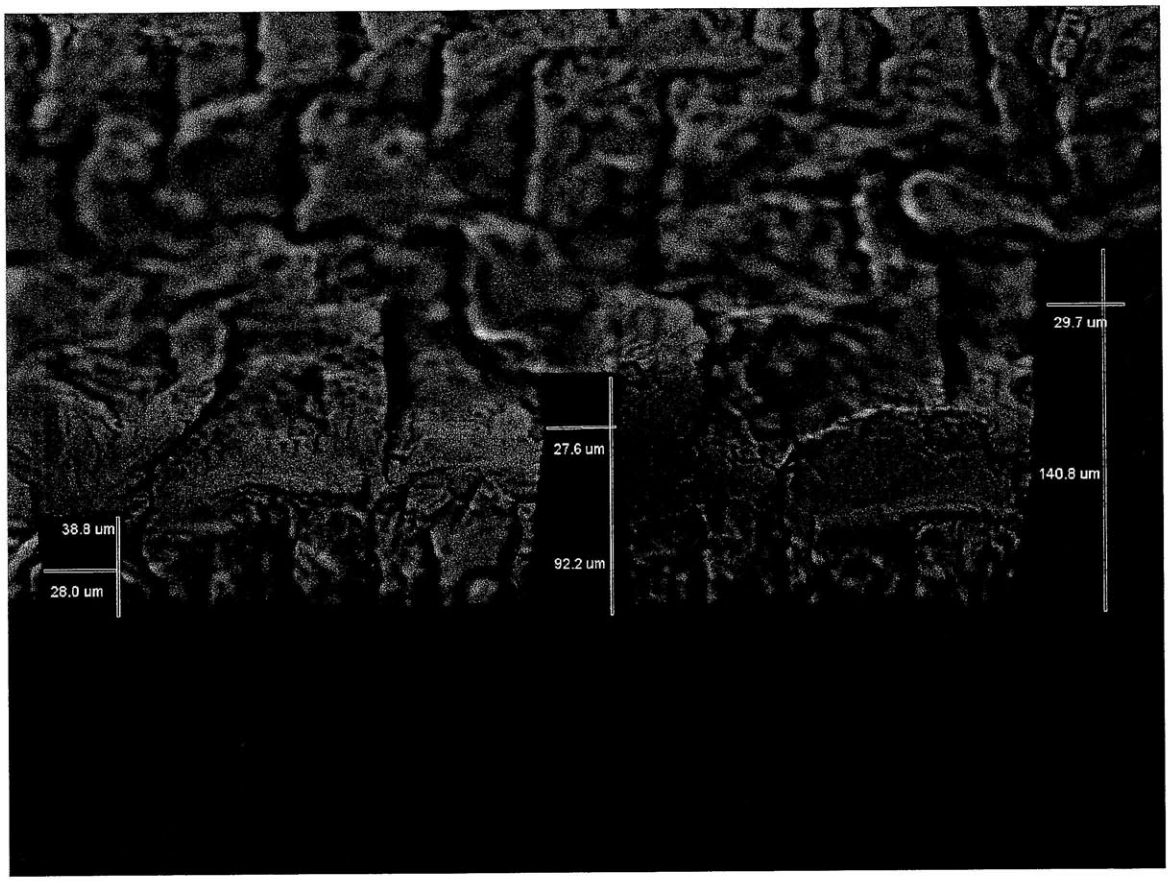

Figure 3-5: Tool offset calibration test for 25 μm endmill

to remove any debris or leftover coolant oil from the machining process. The chip and blank were then dried under nitrogen.

Several bonding techniques were investigated to attach the chip to the blank, including low viscosity acrylic cement, ultrasonic bonding in the presence of methanol, and thermal bonding. All of these techniques were able to bond the chips, but none of them produced high quality devices. The acrylic cement had a tendency to accumulate in the channels, where it would rapidly harden and block them. Ultrasonic bonding and thermal bonding both produced deformations in the channel when conducted at a sufficient temperature or amplitude to induce bonding. Finally, a solvent assisted thermal bonding process adapted from Brown et al. was chosen as the most effective [9].

In this process, 50 μL of a ternary solvent system of 47.5% dimethyl sulfoxide (DMSO), 47.5% deionized water, and 5% methanol was applied to the blank piece of PMMA. The machined chip was placed on top, and then the device was clamped together in an aluminum fixture. The fixture was heated in a furnace at 96°C for thirty five minutes, and then the temperature was gradually ramped back to 40°C over another thirty minutes before the device was removed from the furnace. The furnace and clamping fixture are shown in figure 3-6. After the device was removed from the fixture, water was flushed through all the channels in order to remove any remaining bonding solvent. This process produced complete and irreversible bonding with no observed thermal deformation

Once the devices were cool and dry, fluid reservoirs were attached to the chip. The reservoirs had a volume of 70 μL, which was sufficient to eliminate any variation in pH over the course of the experiment [71]. They were attached to the chip using Devcon five-minute epoxy. A completed chip (with two sets of reservoirs attached) is shown in figure 3-7. A detailed analysis of the performance of the device is described in chapter 4, as well as in the literature [8]. Experimental data are presented in chapter 5.

Figure 3-6: Bonding apparatus for solvent-assisted bonding of PMMA microfluidic devices

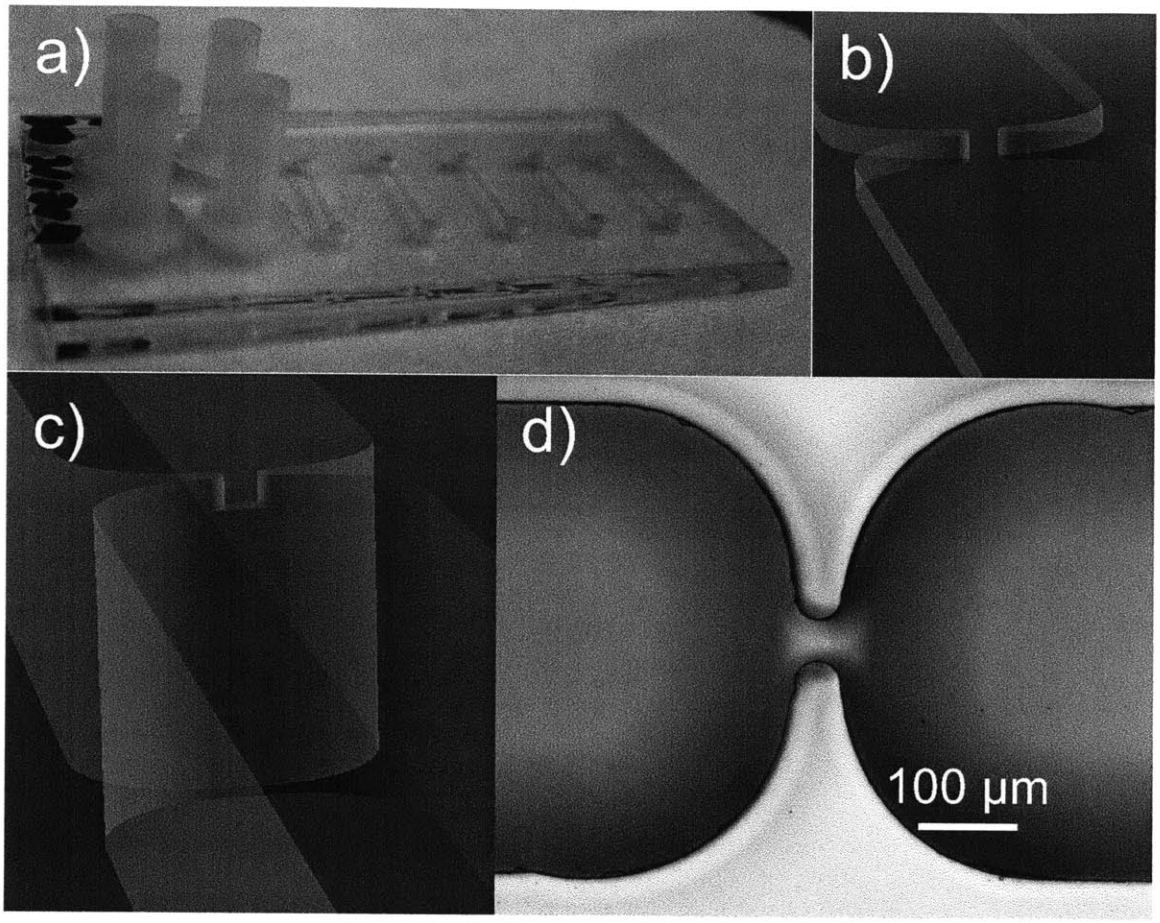

Figure 3-7: (a) Completed 3DiDEP device, with two sets of reservoirs attached. (b + c) Computer renderings of the 2D and 3D constriction regions. (d) Micrograph of constriction region from 3DiDEP device

Chapter 4

Modeling of 3DiDEP Devices

4.1 Introduction

Having discussed the underlying physics of dielectrophoresis (DEP) in chapter 2 and the specific design of the three-dimensional insulator-based dielectrophoresis (3DiDEP) device in chapter 3, it is helpful to understand the effects of DEP when applied to insulator-based dielectrophoresis (iDEP) devices in general, and the electroosmostically driven 3DiDEP device presented here in particular. Since the purpose of these devices is to trap microparticles based on their dielectric properties, the clearest way to look at the system is in terms of how the different forces acting on the particles will contribute to the net velocity of the particle. Since thermal effects may also be significant, the temperature field in the system must be considered as well [32]. This approach will allow for the identification of critical performance metrics for the system. Next, analytical approximations are made in order to create a working intuition for the performance of the device. Fully three-dimensional numerical simulation of the device were also performed and predictions for trapping performance and temperature variations are presented.

4.2 Drag on Particles in Microfluidic Channels

In order for the approach outlined in the previous section to be valid, it must be the case that velocity is proportional to force:

$$\mathbf{F} \propto \mathbf{v}. \tag{4.1}$$

This requirement is satisfied in the case of low Reynolds number flow, which is typically defined in terms of the characteristic velocity U, length scale w, and kinematic viscosity ν of a system as $\mathrm{Re}_w = Uw/\nu \ll 1$. Although microfluidic devices typically have very low Reynolds numbers, it is always wise to check. For electromosotically driven flow, the bulk fluid velocity $U \approx \mu_{EO}\phi_0/L$, where $\mu_{EO} = 1.1\times10^{-8}$ m^2/Vs is the electroosmotic mobility of an aqueous solution with neutral pH against poly(methyl methacrylate) (PMMA), ϕ_0 is the applied voltage, and $L = 1$ cm is the channel length [18]. For the 3DiDEP device presented here with applied voltage $\phi_0 = 10 - 100$ V, the Reynolds number can be written as

$$\begin{aligned} &= \frac{\mu_{EO}\phi_0 w}{\nu L} \\ &= 0.006 - 0.063. \end{aligned} \tag{4.2}$$

This easily satisfies the low Reynolds number requirement of Stokes flow, so particles with thin double layers surrounded by fluid of dynamic viscosity η can be said to respond linearly to forces as required. In the case of a sphere:

$$\mathbf{F} = 6\pi\eta r\mathbf{v}. \tag{4.3}$$

Slight corrections to this equation exist for ellipsoidal particles, but the general behavior is exactly the same [2]. For the case of a prolate ellipsoid with minor semiaxis b , Stokes drag can be written as [89]:

$$\mathbf{F} = 8\pi\beta\eta r\mathbf{v} \tag{4.4}$$

$$\beta = \frac{1}{\ln(4/\mathrm{Re}_w) - \gamma + 1/2}.$$

Euler's constant is $\gamma = 0.5772$. In this case, β is a weak function of Reynolds number. Figure 4-1 compares the friction factor $f = F/(\pi\eta r v)$ for a sphere and prolate ellipsoid with eccentricity $\epsilon = \sqrt{1-(a_1/a_2)^2} = 0.97$, which is typical of an *Escherichia coli* bacterium. It is reasonable based on this result to consider the case of rod-shaped particles as an extension of spherical particles. For this reason, all derivations shown here will be for spherical particles, with the understanding that no new physics is added when the shape of the particle changes.

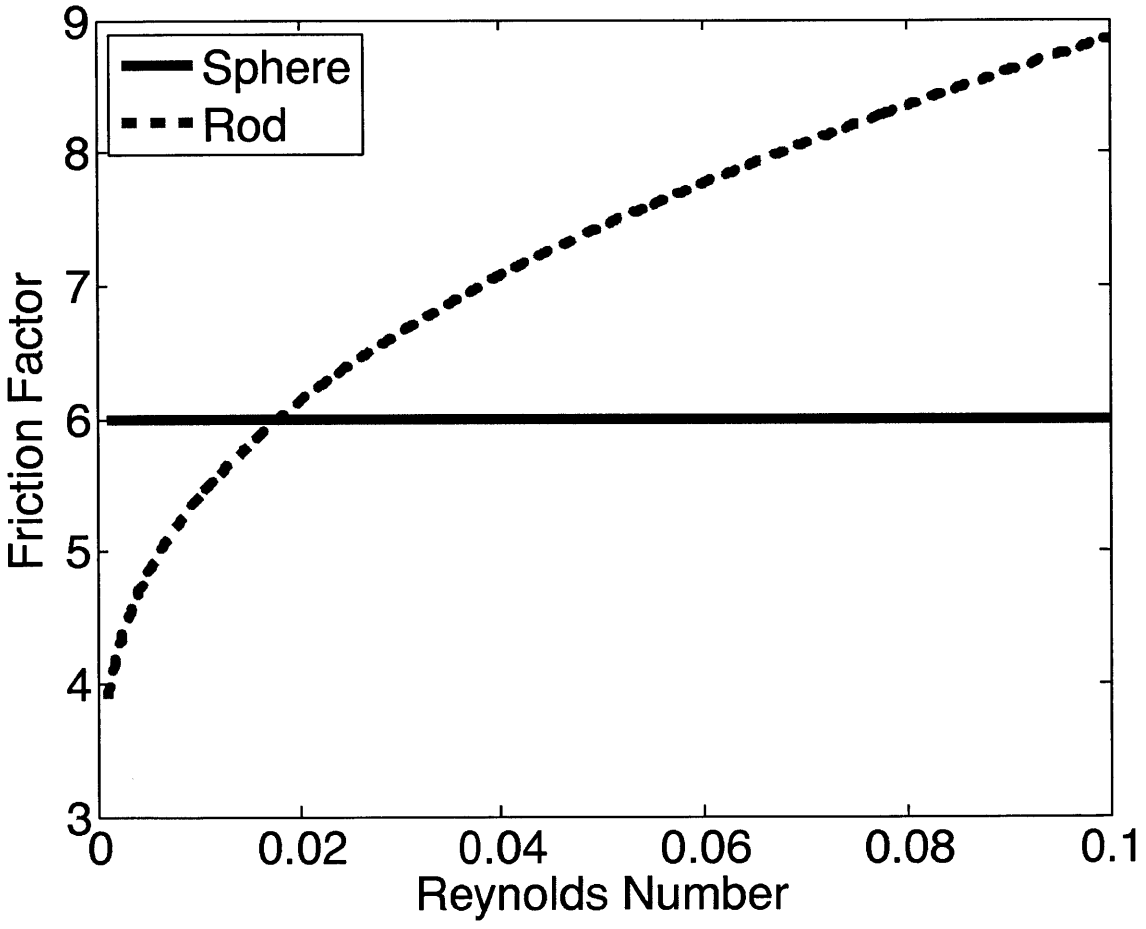

Figure 4-1: Comparison of friction factors for a sphere and a prolate ellipsoid.

4.3 Force Balance in iDEP

There are three major effects that impact the motion of particles in iDEP devices: electroosmosis, electrophoresis, and dielectrophoresis. Electroosmosis is caused by a nonzero surface charge at the wall of the channel. When a DC voltage is applied across the channel, the resultant electric field acts on the charge that has accumulated in the double layer near the channel walls, causing a net fluid flow. Since the double layer for the electrolytes employed here is extremely thin, this effect results in a slip velocity $\mathbf{v}_{wall}$ along the walls of the channel. The velocity is proportional to the tangential electric field $\mathbf{E}_{wall}$ and the electroosmotic mobility μ_{EO}:

$$\mathbf{v}_{wall} = \mu_{EO}\mathbf{E}_{wall}. \tag{4.5}$$

This slip velocity serves as a boundary condition in deriving the fluid velocity profile $\mathbf{v}_{fl}$ within the channel.

The second important effect is that of electrophoresis. Assuming that the particles themselves also have a nonzero surface charge, they will experience a net force due to the applied DC field. This effect can be expressed in terms of the electrophoretic mobility of the particle:

$$\mathbf{v}_{EP} = -\mu_{EP}\mathbf{E}. \tag{4.6}$$

The third effect, dielectrophoresis, is most important near the constriction region, where the field gradient is large. The force experienced by a particle due to dielectrophoresis is described by equation 2.10. For Stokes flow, we can substitute this expression into equation 4.3 to obtain:

$$\begin{aligned} \mathbf{v}_{DEP} &= \frac{\mathbf{F}_{DEP}}{6\pi\eta r} \\ &= \frac{\varepsilon_m \kappa_{CM} r^2}{3\eta}\nabla E^2 \\ &= \mu_{DEP}\nabla E^2 \end{aligned} \tag{4.7}$$

$$\mu_{DEP} = \frac{\varepsilon_m \kappa_{CM} r^2}{3\eta},$$

where η is viscosity, ε_m is the media permittivity, r is the particle radius, μ_{DEP} is the dielectrophoretic mobility, and κ_{CM} is the Clausius-Mossotti factor.

When all three of these effects are considered together, it is possible to obtain an expression for the net velocity of a particle in the channel. As long as interparticle effects are neglected, which is a reasonable assumption for dilute suspensions:

$$\mathbf{v}_{NET} = \mathbf{v}_{fl} + \mathbf{v}_{EP} + \mathbf{v}_{DEP}. \tag{4.8}$$

For a device whose primary function is trapping, being able to predict exactly where in the channel the particles accumulate is of particular utility. It must be noted that once the particles accumulate in the trapping regions, interparticle effects do become important, and can produce interesting phenomena [31]. However, these phenomena will not be considered in this work. One approach to predicted the trapping regions is to make the assumption that particles travel along electric field lines, and then to look for stagnation points along those lines [33]. It is convenient to define a trapping parameter α that represents the ratio between DEP velocity parallel to the electric field and all other particle motion parallel to the electric field.

$$\alpha \equiv \frac{\mathbf{v}_{DEP} \cdot \mathbf{E}}{(\mathbf{v}_{fl} + \mathbf{v}_{EP}) \cdot \mathbf{E}}. \tag{4.9}$$

Where $\alpha = 1$, particles have reached a stagnation point, and cannot travel any further along the field lines. The requirement that $\alpha \geq 1$ then defines the trapping region. Substituting equations 4.7 and 4.8 into equation 4.9 yields a working expression for trapping parameter:

$$\alpha = \frac{\mu_{DEP} \nabla E^2}{\mathbf{v}_{fl} \cdot \mathbf{E} - \mu_{EP} E^2} \cdot \mathbf{E}. \tag{4.10}$$

This dimensionless constant provides a clear figure of merit for all iDEP designs. It incorporates all of the critical dependencies present in iDEP, and can be used to

determine if particles will trap in a particular device under specific conditions.

4.4 Dimensional Analysis

For a complex three-dimensional system such as the 3DiDEP device, exact analytical solutions for α do not exist. In addition, the question of heat transfer in the device must also be considered. Before resorting to a full numerical model of the device, a great deal of information can be gleaned analytically. The first step is to perform a dimensional analysis of the problem using the Buckingham Pi theorem. The relevant parameters for the problem are the channel length L and width W, constriction width w, applied voltage ϕ_0, electroosmotic mobility μ_{EO}, media conductivity σ, viscosity η, volumetric heat capacity ρc_p, and thermal conductivity k. There are four field variables of interest: pressure $P(\mathbf{x})$, temperature $T(\mathbf{x})$, fluid velocity $\mathbf{u}(\mathbf{x})$, and current density $\mathbf{J}(\mathbf{u})$. In a most general sense, then, the problem can be expressed as:

$$(P(\mathbf{x}), T(\mathbf{u}), \mathbf{u}(\mathbf{x}), \mathbf{J}(\mathbf{x})) = F(L, W, w, \phi_0, \mu_{EO}, \sigma, \eta, \rho c_p, k) \tag{4.11}$$

First express the parameters and variables of the problem in terms of their fundamental dimensions: mass M, length L, time T, temperature Θ, and charge Q:

$$\begin{aligned}
P(\mathbf{x}) \quad [=] \quad & \frac{M}{LT^2} \\
T(\mathbf{x}) \quad [=] \quad & \Theta \\
\mathbf{u}(\mathbf{x}) \quad [=] \quad & \frac{L}{T} \\
\mathbf{J}(\mathbf{x}) \quad [=] \quad & \frac{Q}{L^2 T} \\
L \quad [=] \quad & L \\
W \quad [=] \quad & L \\
w \quad [=] \quad & L \\
\phi_0 \quad [=] \quad & \frac{ML^2}{QT^2} \\
\mu_{EO} \quad [=] \quad & \frac{QT}{M}
\end{aligned}$$

$$\begin{aligned}
\sigma \quad [=] \quad & \frac{Q^2T}{ML^3} \\
\eta \quad [=] \quad & \frac{M}{LT} \\
\rho c_p \quad [=] \quad & = \frac{M}{LT^2\Theta} \\
k \quad [=] \quad & \frac{ML}{T^3\Theta}
\end{aligned}$$

There are twelve variables and five dimensions to the problem, so it is possible to use the Buckingham Pi Theorem to write the problem in dimensionless form with only eight variables:

$$(\Pi_1, \Pi_2, \Pi_3, \Pi_4) = \Phi(\Pi_5, \Pi_6, \Pi_7, \Pi_8). \tag{4.12}$$

Define L, η, μ_{EO}, σ, and k as the five repeating variables, which leaves eight dimensionless groups. The dimensional matrix for our set of five repeating variables can be written as:

$$\begin{aligned}
\mathbf{A} &= \begin{bmatrix} [L] & [\eta] & [\mu_{EO}] & [\phi_0] & [k] \end{bmatrix} \\
&= \begin{bmatrix} 0 & 1 & -1 & 1 & 1 \\ 1 & -1 & 0 & 2 & 1 \\ 0 & -1 & 1 & -2 & -3 \\ 0 & 0 & 0 & 0 & -1 \\ 0 & 0 & 1 & -1 & 0 \end{bmatrix}.
\end{aligned} \tag{4.13}$$

The dimensions of the remaining eight variables are then assembled into a matrix:

$$\mathbf{B} = \begin{bmatrix} [P] & [T] & [\mathbf{u}] & [\mathbf{J}] & [W] & [w] & [\rho c_p] & [\sigma] \end{bmatrix}$$

$$= \begin{bmatrix} 1 & 0 & 0 & 0 & 0 & 0 & 1 & -1 \\ -1 & 0 & 1 & -2 & 1 & 1 & -1 & -3 \\ -2 & 0 & -1 & -1 & 0 & 0 & -2 & 1 \\ 0 & 1 & 0 & 0 & 0 & 0 & -1 & 0 \\ 0 & 0 & 0 & 1 & 0 & 0 & 0 & 2 \end{bmatrix} \tag{4.14}$$

In order for the entire system to be dimensionless, the dimensional units must all cancel out. This can be expressed in matrix form:

$$\mathbf{AX} + \mathbf{B} = 0. \tag{4.15}$$

It is straightforward to solve for the units matrix X:

$$\mathbf{X} = \begin{bmatrix} 2 & 2 & 1 & 3 & -1 & -1 & 0 & 2 \\ -1 & -1 & 0 & -1 & 0 & 0 & 0 & -1 \\ -1 & -2 & -1 & -2 & 0 & 0 & 1 & -2 \\ -1 & -2 & -1 & -1 & 0 & 0 & 1 & 0 \\ 0 & 1 & 0 & 0 & 0 & 0 & -1 & 0 \end{bmatrix}. \tag{4.16}$$

This result can be used to reform the general problem statement in dimensionless form:

$$\left(\frac{L^2P}{\eta\mu_{EO}\phi_0}, \frac{kL^2T}{\eta\mu_{EO}^2\phi_0^2}, \frac{L\mathbf{u}}{\mu_{EO}\phi_0}, \frac{L^3\mathbf{J}}{\eta\mu_{EO}^2\phi_0}\right) = \Phi\left(\frac{W}{L}, \frac{w}{L}, \frac{\mu_{EO}\rho c_p\phi_0}{k}, \frac{L^2\sigma}{\eta\mu_{EO}^2}\right) \tag{4.17}$$

Since σ is a known parameter in the experiment, it is convenient to simplify by dividing the dimensionless temperature Π_2 and dimensionless current Π_4 by the dimensionless conductivity Π_8. If we then recognize that Π_7 is simply the axial Peclet number Pe_L, then the problem statement can be simplified to the following form:

$$\left(\frac{L^2P}{\eta\mu_{EO}\phi_0}, \frac{kT}{\sigma\phi_0^2}, \frac{L\mathbf{u}}{\mu_{EO}\phi_0}, \frac{L\mathbf{J}}{\sigma\phi_0}\right) = \Phi\left(\frac{W}{L}, \frac{w}{L}, \mathrm{Pe}_L, \frac{L^2\sigma}{\eta\mu_{EO}^2}\right). \tag{4.18}$$

This analysis leaves us with smaller number of experimental parameters and provides meaningful scales for the variables of the problem:

$$\begin{aligned} U_0 &= \frac{\mu_{EO}\phi_0}{L} \\ P_0 &= \frac{\eta\mu_{EO}\phi_0}{L^2} \\ T_0 &= \frac{\sigma\phi_0^2}{k} \\ J_0 &= \frac{\sigma\phi_0}{L}. \end{aligned} \tag{4.19}$$

4.5 Governing Equations

Now that the key scales of the problem are defined, we can directly consider the differential equations that govern the system. For the purpose of estimating the most important behaviors, density, heat capacity, viscosity, thermal conductivity and ionic conductivity are treated as constants. The following equations govern fluid flow, heat transfer, and current conservation:

$$0 = -\nabla p + \eta\nabla^2\mathbf{u} \tag{4.20}$$

$$\rho C_p\mathbf{u}\cdot\nabla T = k\nabla^2 T + \frac{\mathbf{J}\cdot\mathbf{J}}{\sigma} \tag{4.21}$$

$$0 = \nabla\cdot\mathbf{J}. \tag{4.22}$$

The scaled values from equation 4.19 can now be used define the following dimensionless variables:

$$\begin{aligned} \tilde{\mathbf{x}} &= \frac{\mathbf{x}}{L} \\ \tilde{\mathbf{u}} &= \frac{L\mathbf{u}}{\mu_{EO}\phi_0} \\ \tilde{P} &= \frac{L^2 P}{\eta\mu_{EO}\phi_0} \\ \tilde{T} &= \frac{k(T-T_a)}{\sigma\phi_0^2} \\ \tilde{\mathbf{J}} &= \frac{L\mathbf{J}}{\sigma\phi_0}. \end{aligned}$$

When these dimensionless quantities are substituted into the governing equations, they become:

$$0 = \tilde{\nabla}\tilde{P} + \tilde{\nabla}^2\tilde{\mathbf{u}} \tag{4.23}$$

$$\mathrm{Pe}_L\ \tilde{\mathbf{u}} \cdot \tilde{\nabla}\tilde{T} = \tilde{\nabla}^2\tilde{T} + \tilde{\mathbf{J}} \cdot \tilde{\mathbf{J}} \tag{4.24}$$

$$0 = \nabla \cdot \tilde{\mathbf{J}} \tag{4.25}$$

Where

$$\mathrm{Pe}_L \equiv \frac{\mu_{EO}\rho C_p \phi_0}{k}.$$

Only the Peclet number remains as a dimensionless parameter. It is also useful to apply the scales from equation 4.19 to trapping parameter α, which is defined by equation 4.10. Assuming that the electric field changes most strongly over a distance equal to the constriction width a, the maximum trapping parameter along the centerline of the channel for a particle of radius r in a channel with constriction ratio $W^2/w^2 = \chi$ can be estimated to be:

$$\alpha_{scale} \approx \frac{\varepsilon \kappa_{CM} r^2}{3\eta(\mu_{EO} - \mu_{EP})} \frac{\phi_0 \chi}{Lw}. \tag{4.26}$$

When $\alpha_{scale} > 1$, trapping is predicted, and when $\alpha_{scale} < 1$, it is not. This relatively simple expression takes into account four different three-dimensional field variables, and as will be shown later, achieves good agreement with numerical simulations and experiment. Although further modeling will be necessary to answer other important questions, such as exactly where trapping occurs, this expression provides intuition for how the system performs, and will be a very useful comparison tool for results from more complex numerical simulations.

4.6 Boundary Conditions

First define the boundary conditions in terms of dimensional quantities. The exact geometry of the system will be important, but for now, the system boundary can be divided into three pieces. At the inlet and outlet, the potentials are held at ϕ_0 and ground, respectively. There is no applied stress at either end. The thermal boundary conditions at the inlet and outlet are potentially complicated, since some transient heating behavior will occur there. In order to avoid introducing unnecessary time-dependence to the system, note that the reservoirs can be considered lumped thermal systems since their Biot number is

$$\text{Bi} = \frac{hV}{kA} \approx \frac{10\pi r}{2k} = 0.013. \tag{4.27}$$

Their characteristic response time is then:

$$\tau = \frac{\rho c_v V}{hA_s} \approx \frac{10^3 \cdot 4181 \cdot r}{2h} = 300 \text{ seconds}. \tag{4.28}$$

Since a typical experiment only runs for about thirty seconds, the reservoirs can be considered isothermal throughout the course of an experiment. This greatly simplifies the problem, and allows for more flexibility in the selection of solution methods. The walls of the channel are electrically insulating with electroosmotic slip as described by equation 4.5. In order to determine the thermal boundary conditions along the walls, consider the series resistances per unit area to heat flux through the PMMA and to the outside air. The PMMA on the top and bottom of the channel is roughly 1 mm thick, with thermal conductivity $k_{PMMA} = 0.2$ W/(mK). Assuming a convective heat transfer coefficient to still air of $h_air = 10$ W/m^{2}K:

$$\begin{aligned} R_{PMMA} &= \frac{0.001}{0.2} = 0.005 \\ R_{air} &= \frac{1}{10} = 0.1. \end{aligned}$$

Clearly convective heat transfer to the air is the limiting factor, so conduction through the PMMA can be treated as fast and neglected. The situation is slightly more complicated at the sidewalls of the channels, since the heat must travel through a much longer length of PMMA before transferring to the surrounding air. A quick check of the Biot number for a 3 mm thick chip ($\frac{hA}{kP} \approx 0.15 < \frac{1}{6}$) shows that it is reasonable to treat the 7 mm length of PMMA between channels as a quasi one-dimensional fin. In this case, the effective heat transfer coefficient on the sidewalls of the channel can be calculated simply using the result for a fin of finite length:

$$h_{fin} = h_{air}\sqrt{\frac{k_{PMMA}P}{h_{air}A}}\tanh\left(\sqrt{\frac{h_{air}P}{k_{PMMA}A}}L\right) = 3.13h_{air} \approx 31.3\ \frac{\mathrm{W}}{\mathrm{m^2K}}. \qquad (4.29)$$

This fully specifies the problem statement for this system.

4.7 One Dimensional Thermal Approximation

It is non-trivial to solve the full system of boundary conditions and coupled partial differential equations for a 3DiDEP channel as specified in sections 4.5 and 4.6. A numerical solution is presented in section 4.8 that solves the complete problem for both the 2DiDEP and 3DiDEP models, but more information can still be extracted analytically. In particular, the temperature scale described by equation 4.19 does not take into account heat generation due to the channel constriction, which in many cases is the dominant source of heat in the system. Since the governing energy equation has three terms that are potentially of the same order, there is no immediately clear temperature scale for the problem independent of boundary conditions. However, careful examination of the system can be used to make good approximations that allow for some reduction in dimensionality and yield analytic solutions for temperature distribution.

It can be shown that the Biot number for a channel of width W can be written

as:

$$\mathrm{Bi} = \frac{h_{air} W}{4 k_m} \approx 10^{-3}. \tag{4.30}$$

For $\mathrm{Bi} \ll 1/6$, the radial variation in temperature within the channel will be small, so we are justified in treating the channel as being quasi one-dimensional for the purpose of temperature distribution. Since the flow in the channel is due to electroosmosis, the velocity profile will be very close to uniform. It is therefore appropriate to approximate the system as a moving fin with internal heat generation. As discussed in section 4.6, the convective heat transfer coefficients for the channel are approximately 10 W/m^{2}K on the top and bottom and 30 W/m^{2}K on the sides, so when treated as a quasi one-dimensional system, an effective heat transfer coefficient of $h_{\mathrm{fin}} = 20$ W/m^{2}K can be assumed.

The governing equation for the channel far away from the constriction (where $\tilde{J} = \tilde{u} = 1$) can be written in 1-dimension as:

$$\mathrm{Pe}_L \frac{d\tilde{T}}{d\tilde{x}} = \frac{d^2\tilde{T}}{d\tilde{x}^2} - \frac{4 h_{\mathrm{fin}} L^2}{kW} \tilde{T} + 1. \tag{4.31}$$

This is a one-dimensional version of equation 4.23, with an additional term to account for the convective heat loss to the walls of the channel.

The solution can then be divided into two sections $\tilde{T}_1$ and $\tilde{T}_2$ for $x < L/2$ and $x > L/2$, with flux and temperature matching boundary conditions at the center. Assuming heat generation of Q at the center and heat fluxes $F_i = W^2(-k dT_i/dx + u\rho c_v T_i)$ along the length of the channel, the dimensional boundary conditions can be written:

$$\begin{aligned} T_1(0) &= T_a \\ T_1(L/2) &= T_2(L/2) \\ F_1 + Q &= F_2 \end{aligned}$$

$$T_2(L) = T_a. \tag{4.32}$$

For a constriction ratio χ, the heat generation in the constriction can be estimated as $Q = w^3 J_c^2/\sigma = w^3\chi^2\sigma V_0^2/L^2$. The dimensionless boundary conditions can be worked out and simplified:

$$\begin{aligned} \tilde{T}_1(0) &= 0 \\ \tilde{T}_1(1/2) &= \tilde{T}_2(1/2) \\ \left(\frac{d\tilde{T}_1}{d\tilde{x}}\right)_{\tilde{x}=1/2} + \frac{w}{L}\chi &= \left(\frac{d\tilde{T}_2}{d\tilde{x}}\right)_{\tilde{x}=1/2} \\ \tilde{T}_2(1) &= 0. \end{aligned} \tag{4.33}$$

The general solution for equation 4.31 has a relatively simple form. Assuming separate solutions for the regions upstream and downstream of the constriction, the solution can be written as:

$$\begin{aligned} \tilde{T}_1 &= A_1 e^{s_1 x} + A_2 e^{s_2 x} + \frac{kW}{4hL^2} \\ \tilde{T}_2 &= B_1 e^{s_1 x} + B_2 e^{s_2 x} + \frac{kW}{4hL^2}, \end{aligned}$$

where:

$$\begin{aligned} s_1 &= -\frac{1}{2}\left(\sqrt{\mathrm{Pe}^2 + \frac{16hL^2}{kW}} - \mathrm{Pe}\right) \\ s_2 &= = \frac{1}{2}\left(\sqrt{\mathrm{Pe}^2 + \frac{16hL^2}{kW}} + \mathrm{Pe}\right) \end{aligned} \tag{4.34}$$

To solve for the coefficients, substitute the general solution into the boundary conditions:

$$\begin{aligned} A_1 + A_2 + \frac{kW}{4hL^2} &= 0 \\ A_1 e^{s_1/2} + A_2 e^{s_2/2} &= B_1 e^{s_1/2} + B_2 e^{s_2/2} \\ s_1 A_1 e^{s_1/2} + s_2 A_2 e^{s_2/2} + \frac{w}{L}\chi &= s_1 B_1 e^{s_1/2} + s_2 B_2 e^{s_2/2} \\ B_1 e^{s_1} + B_2 e^{s_2} + \frac{kW}{4hL^2} &= 0. \end{aligned} \tag{4.35}$$

This system of equations can be written in matrix form:

$$\begin{bmatrix} 1 & 1 & 0 & 0 \\ e^{s_1/2} & e^{s_2/2} & -e^{s_1/2} & -e^{s_2/2} \\ s_1 e^{s_1/2} & s_2 e^{s_2/2} & -s_1 e^{s_1/2} & -s_2 e^{s_2/2} \\ 0 & 0 & e^{s_1} & e^{s_2} \end{bmatrix} \begin{bmatrix} A_1 \\ A_2 \\ B_1 \\ B_2 \end{bmatrix} = \begin{bmatrix} -\frac{kW}{4hL^2} \\ 0 \\ -\frac{w\chi}{L} \\ -\frac{kW}{4hL^2} \end{bmatrix}. \tag{4.36}$$

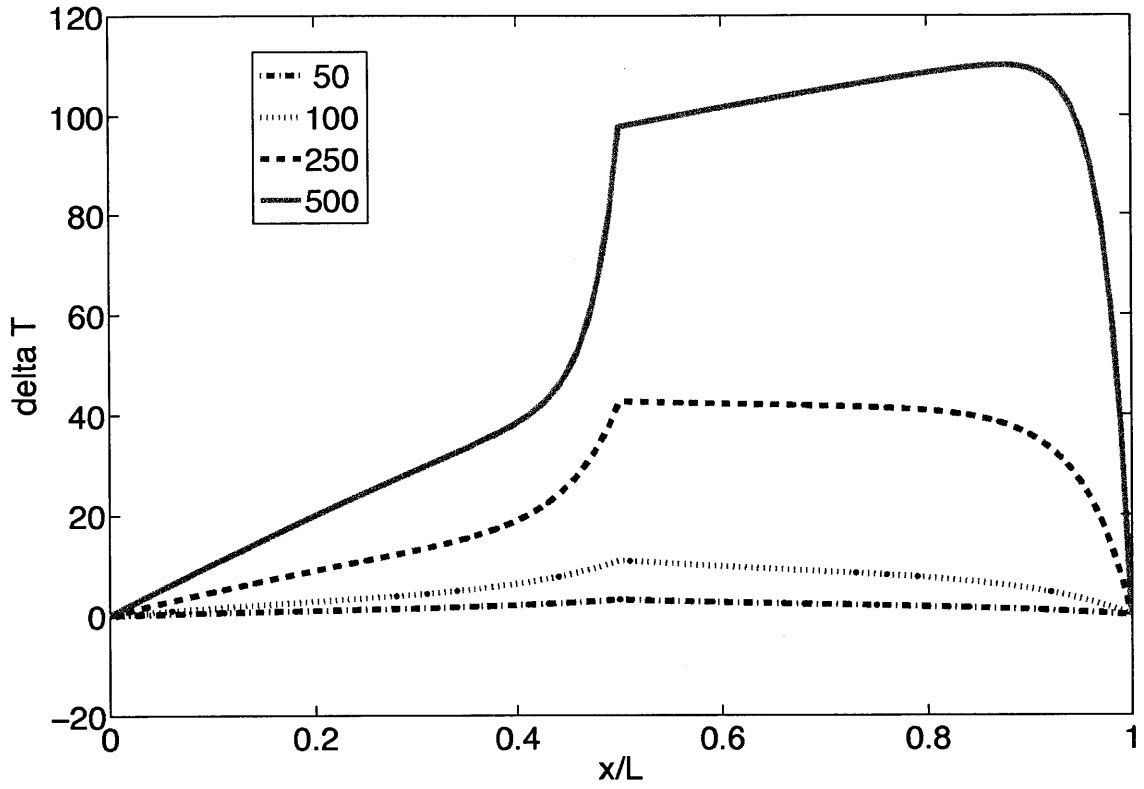

Figure 4-2: Temperature profile as a function of applied voltage along the length of a 3DiDEP channel, calculated using a quasi-1D fin approximation

This equation can be solved easily using a computer algebra system. Figure 4-2 shows how the temperature profile changes for different values of ϕ_0.

4.8 Numerical Model

Numerical models of both the two and three-dimensional iDEP chips were constructed using COMSOL Multiphysics, a finite element commercial software package. Because

dielectrophoresis is a function of electric field squared, small errors in electrical potential propagate into large errors in net forces on particles. It is therefore very important to have a sufficiently fine mesh, particularly in the region near the constriction where dielectrophoresis is important. In addition, in order to accurately model the heat transfer within the channel, three-dimensional geometries are needed for both devices. A number of numerical models of iDEP devices have been presented before, but to the author's knowledge, this is the first work to model iDEP in three dimensions [33, 105, 44, 1, 5].

In order to successfully model the devices in three dimensions with sufficient resolution, it is necessary to pursue the correct solution method. Equations 4.23 are clearly coupled, but fully coupled, nonlinear solvers are extremely resource intensive, and convergence is often a challenge. In order to reduce the computational expense of the model, it is advantageous to observe that the coupling between the equations is essentially unidirectional: temperature distribution is a function of both electric field and fluid velocity, but fluid velocity is only a function of electric field, and electric field is independent of both temperature and fluid velocity. An iterative solver takes advantage of this unidirectionality, and allows for much greater resolution given the computational constraints. The validity of this approach rests on the assumption that fluid properties are homogeneous throughout the system, which is a reasonable assumption for small variations in temperature. Under certain conditions, these assumptions break down, as would be the case if electrothermal flows were significant [32]. However, since the systems studied here are intended for handling biological particles that must be kept within a narrow temperature range, this estimation is justified. Computational expense can be reduced further by applying a symmetry boundary condition down the center $x - z$ plane of the channel and only modeling half of the system. Tetrahedral meshes were generated with approximately 40,000 elements for both devices. This minimized any artifacts due to numerical limitations, and allowed for a solution time of roughly three minutes. The highest density of elements was reserved for the region near the constriction. Figure 4-3 shows the meshes employed in the numerical model. The close-up images shown on the right

demonstrate the higher mesh density in the region nearest the constriction, where dielectrophoresis is most prevalent.

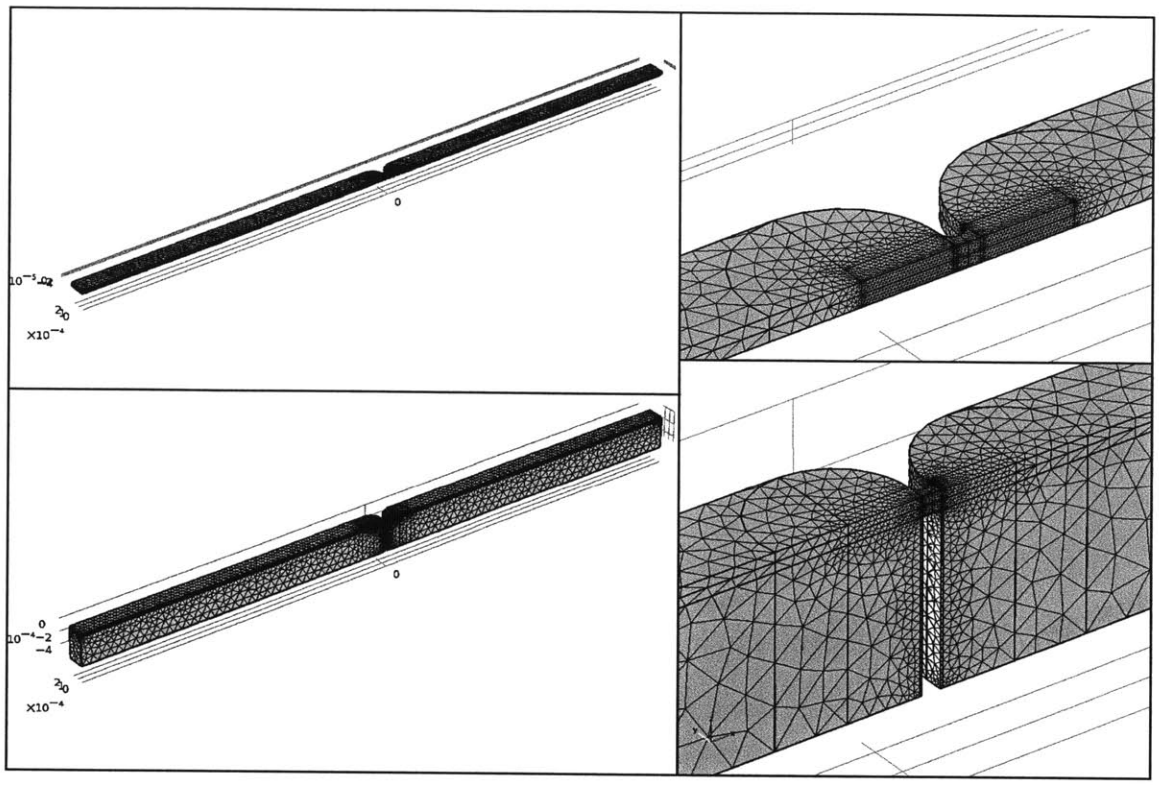

Figure 4-3: Finite element meshes for two and three-dimensional numerical models

Table 4.1 lists the numerical parameters used in model. The electroosmostic mobility was taken from literature, and the electrophoretic mobility was determined experimentally for 10 μm polystyrene beads under the same conditions described in section 5.2 using a Zetasizer zeta potential measurement system [18]. These parameters, along with the governing equations and boundary conditions described earlier fully specify the system for a given applied voltage.

4.9 Numerical Results

One of the most important outputs of this system is a prediction of where particles will trap. This is a matter of calculating α over the entire device geometry. Figure 4-4 shows the predicted trapping zones and particle stream lines in the $x-y$ plane 25 μm

Table 4.1: Parameters for numerical model of iDEP device

Parameter	Value	Description	Units
ε_r	80	relative media permittivity	1
ε_0	8.85×10^{-12}	permittivity of free space	F/m
ρ	10^3	media density	kg/m^2
η	10^{-3}	media viscosity	Pa s
k	0.58	thermal conductivity	W/(m K)
σ_m	100	media conductivity	μS/cm
σ_p	0	particle conductivity	μS/cm
κ_{CM}	$(\sigma_p - \sigma_m)/(\sigma_p + 2\sigma_m)$	Clausius-Mossotti factor	1
r	5	particle radius	μm
c_p	4181	heat capacity	J/(kg K)
μ_{EO}	1.1×10^{-8}	electroosmotic mobility	$m^2/(V\ s)$
μ_{EP}	7.1×10^{-9}	electrophoretic mobility	$m^2/(V\ s)$
μ_{DEP}	$\varepsilon_r\varepsilon_0\kappa_{CM}r^2/(3\eta)$	dielectrophoretic mobility	m^4V^2/s

from the top of a 2DiDEP channel. Note that in these simulations, the particles are assumed to be perfect insulators, as shown in table 4.1, which results in a Clausius-Mossotti factor of -0.5. Under these conditions, trapping occurs upstream of the constriction. At low voltages, small regions form near the lobes of the constriction. This deflects particles that would have stayed near the walls, resulting in focusing of the stream of particles. As the voltage gets larger, the trapping regions grow and eventually meet in the center of the channel. This condition is desirable for trapping, since it ensures that all particles with the desired properties will be immobilized.

The scaling analysis in section 4.5 predicts that trapping occurs in the 3DiDEP device under much lower applied fields than in the 2DiDEP device, so direct comparisons were performed using the numerical model. Figure 4-5 shows the predicted trapping zones and projected particle streamlines in an $x - y$ plan 25 μm from the top of the 3DiDEP channel. Due to the three-dimensional nature of the device, the z component of particle motion is in general nonzero for this system but continuity arguments ensure that it is small near the top of the channel compared the x and y components. As predicted, the required voltages to achieve similar trapping performance in the 3DiDEP device are roughly an order of magnitude lower than those

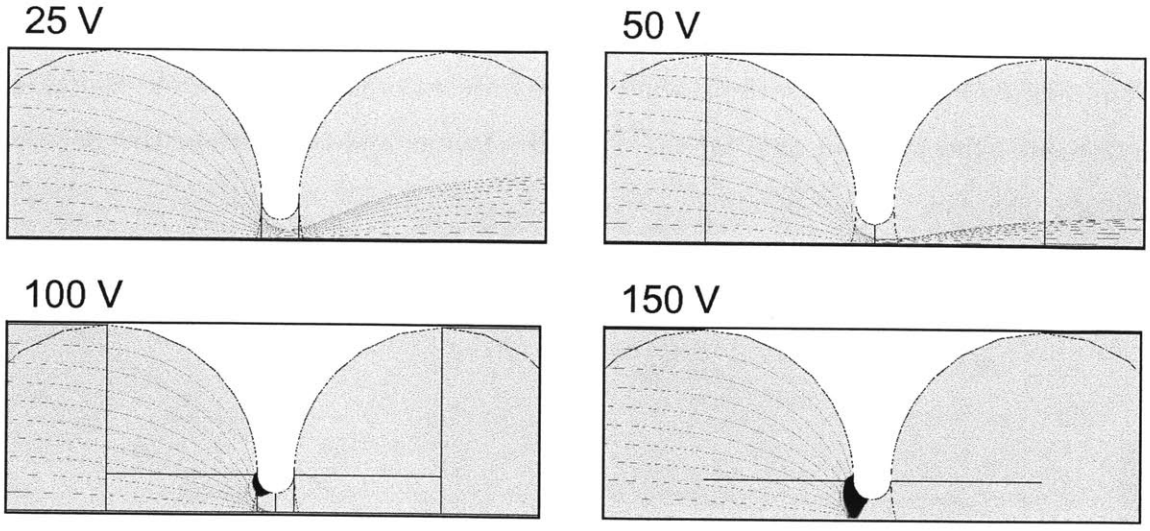

Figure 4-4: Predicted trapping zones and particle streamlines in a 2DiDEP channel

required in the 2DiDEP device.

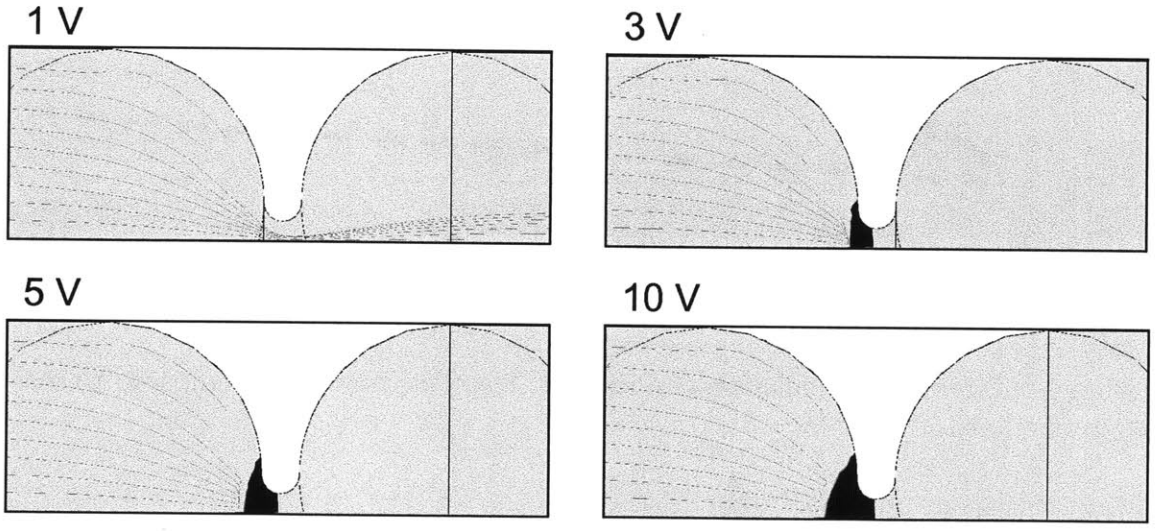

Figure 4-5: Predicted trapping zones and particle streamlines in a 3DiDEP channel

These results make it clear that the last place that trapping occurs in the device is directly in the center of the constriction. Complete trapping can therefore be said to occur when the maximum trapping parameter along the centerline of the constriction, α_{max}, is greater than or equal to one. It is then possible to compile data for α_{max} as a function of applied voltage for both geometries, and to compare them with the scaling analysis described previously. Figure 4-6 shows how the maximum trapping

parameter in the numerical simulation compares to the scaling estimate predictions from section 4.5. Although the scaling law is only an order of magnitude estimate, agreement is better than 15% for the 3DiDEP channel and better than 10% for the 2DiDEP channel.

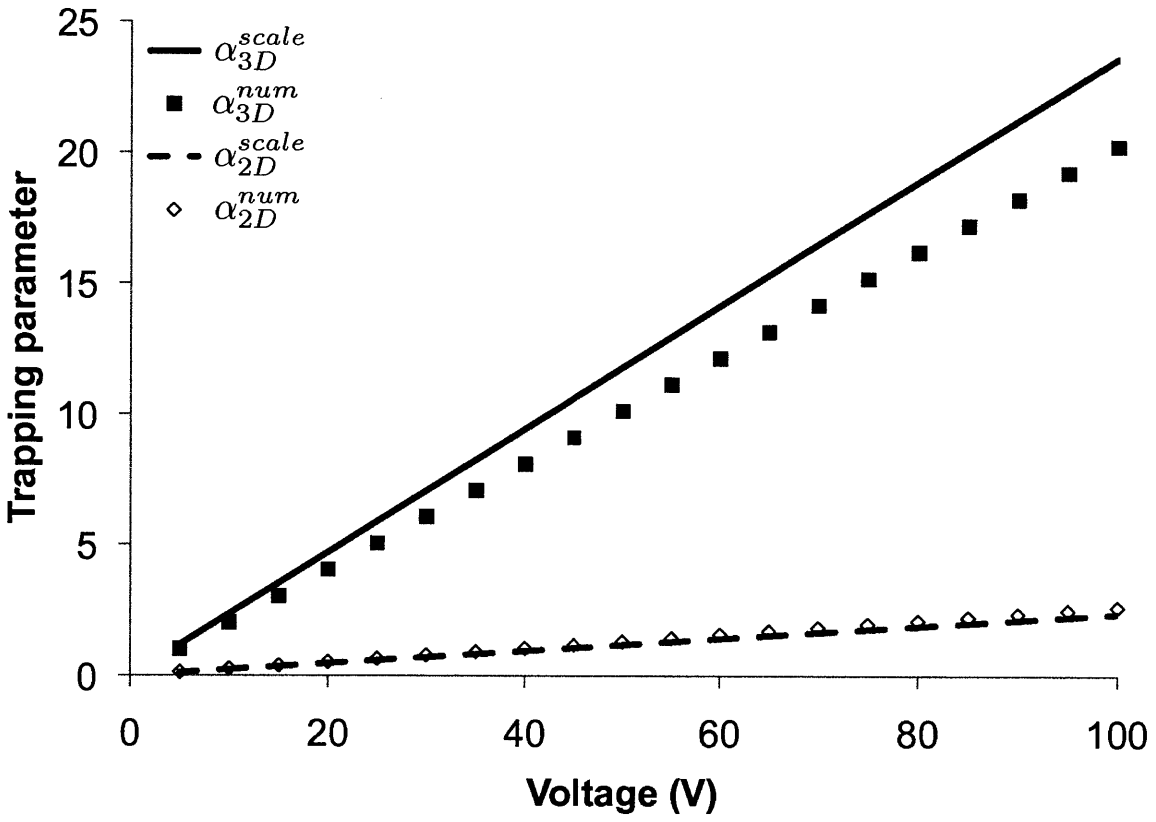

Figure 4-6: Numerical simulation of maximum trapping parameter compared to scaling predictions

Since Joule heating and electrothermal flows are a significant potential problem in many iDEP devices, it is important to consider the temperature distribution across the channel to ensure that such effects are minimized. Figure 4-7 shows how temperature varies along the center $x - z$ plane for both 2D and 3D devices for a maximum predicted trapping parameter of 1.5. As predicted, there is very little temperature variation in the z direction, and temperature variation in the 3D device is an order of magnitude smaller than in the 2D device.

The numerical temperature results can also be compared to the quasi one-dimensional thermal approximation outlined in section 4.7. Figure 4-8 shows how the numerical

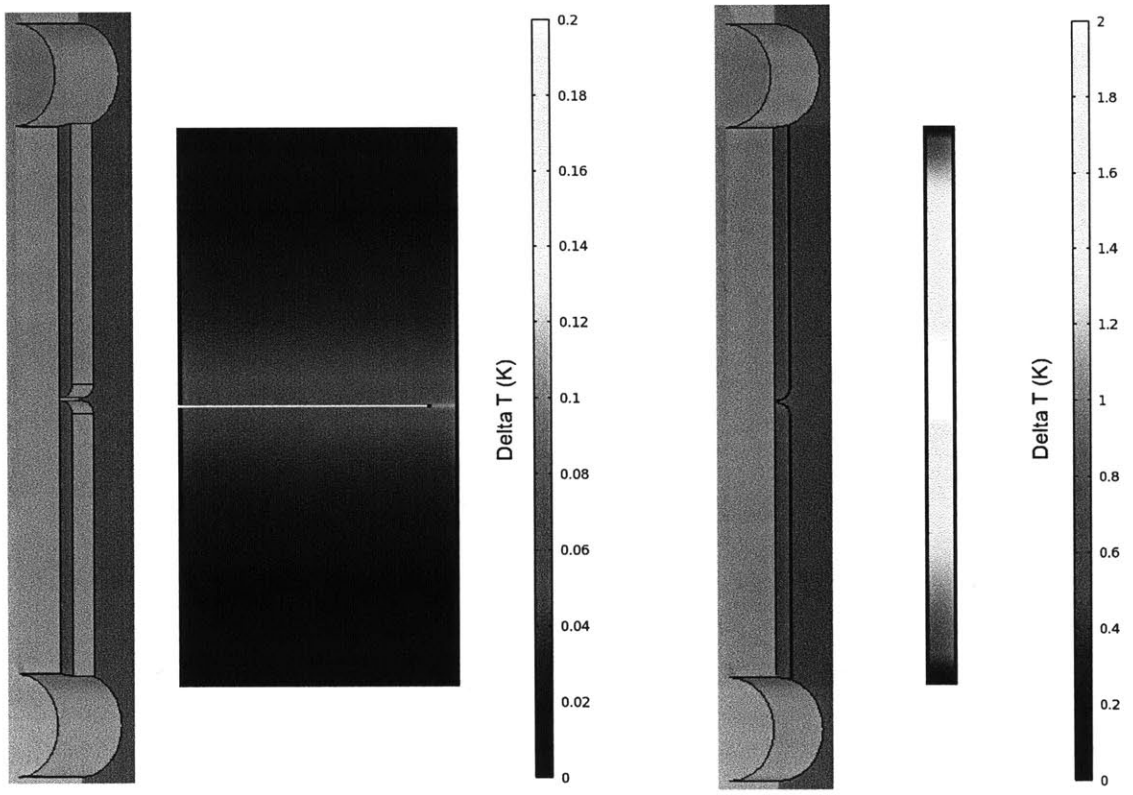

Figure 4-7: Numerical simulation of temperature distribution along the center $x - z$ plane of 3DiDEP (left) and 2DiDEP channels (right)

prediction for maximum temperature varies as a function of applied voltage compared with the quasi one-dimensional approximation. Although not as accurate as the trapping parameter approximations, the dominant trends of the approximation are correct, and provide insight into how the system will perform. Note that although for a given applied voltage, a larger temperature variation is observed in the 3DiDEP channel than in the 2DiDEP channel, the improvement in trapping efficiency more than makes up the difference.

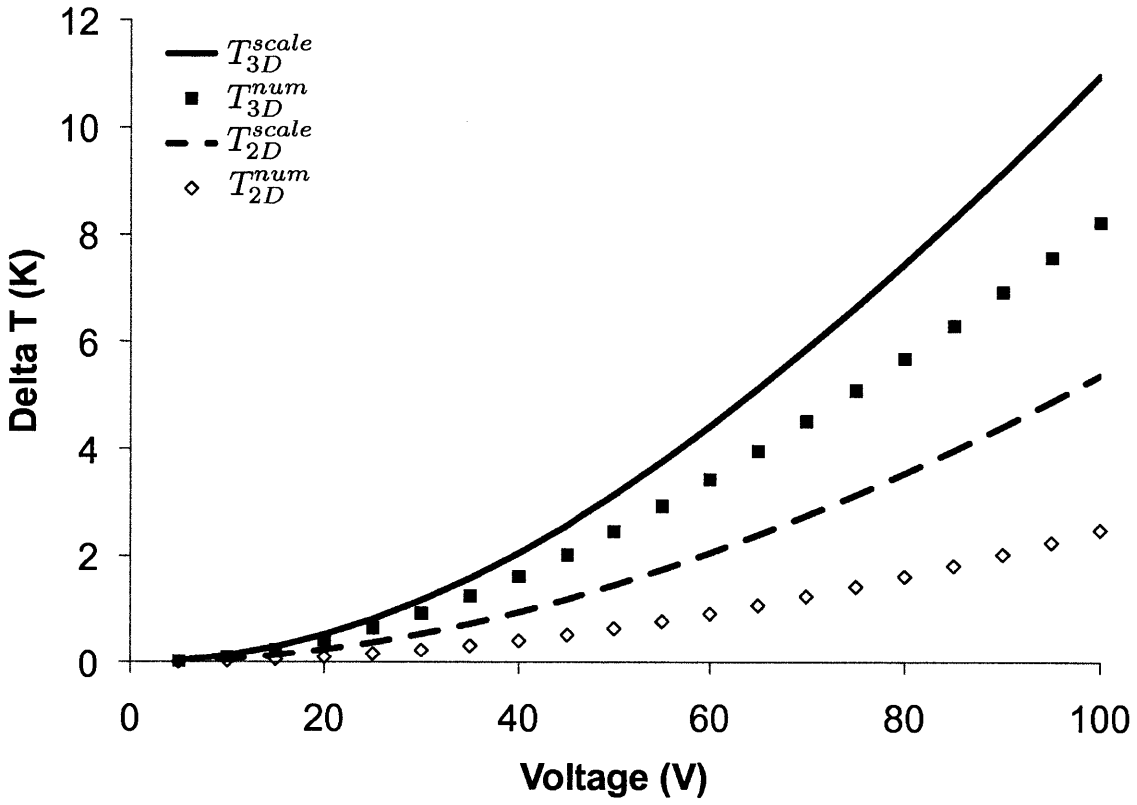

Figure 4-8: Comparison of predicted temperature change in 2DiDEP and 3DiDEP channels from numerical model and quasi one-dimensional model

One of the clear conclusions of the modeling work is the improved performance of the 3DiDEP devices versus the 2DiDEP devices. Figure 4-9 demonstrates that for the same acceptable temperature variation, the 3DiDEP device exhibits much stronger trapping performance according to both the numerical model and scaling analyses. The trapping parameters shown here are for 10 μm insulating beads, in which case either device is capable of acheiving $\alpha_{max} > 1$ within acceptable temperature variations.

However, for smaller particles such as bacteria, the increase in trapping sensitivity will be critical.

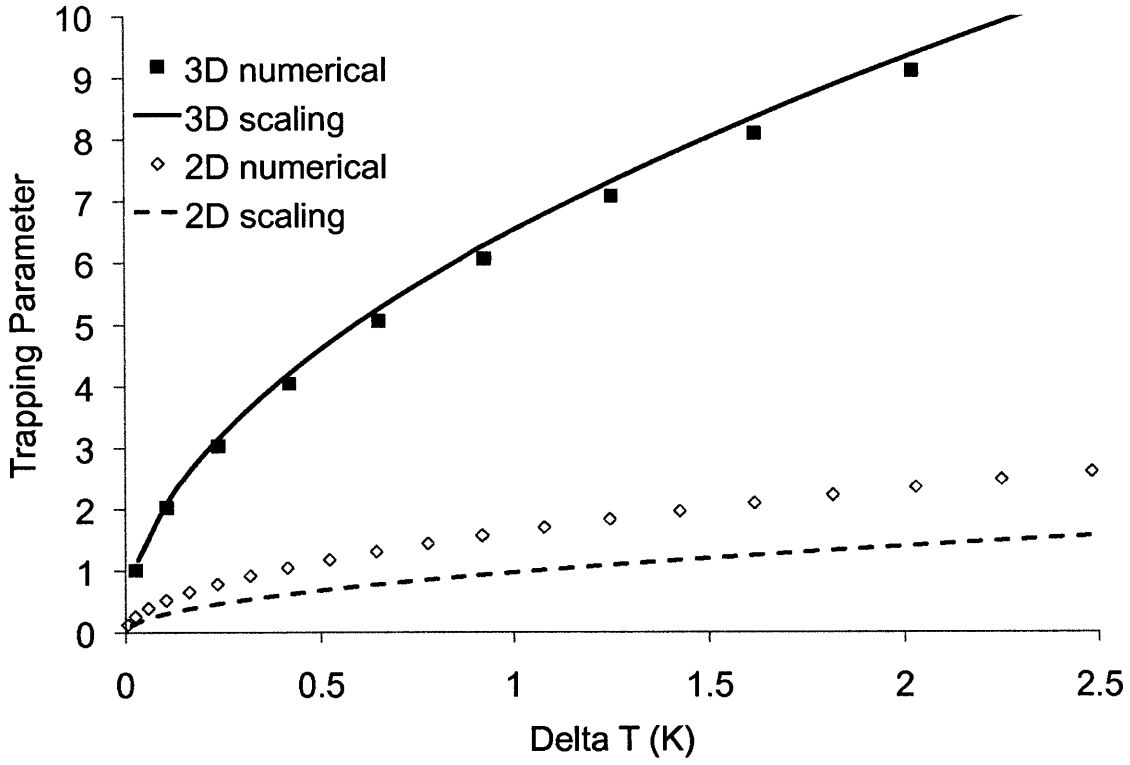

Figure 4-9: Numerical simulation and scaling analysis of maximum trapping parameter in 2DiDEP and 3DiDEP devices compared to numerically predicted and analytically estimated maximum temperature variation

Chapter 5

Trapping of Bacteria and Microparticles

5.1 Introduction

This chapter presents the experimental results obtained using the three-dimensional insulator-based dielectrophoresis (3DiDEP) devices described in chapter 3. In the first set of experiments, polystyrene beads were trapped in the devices to obtain a measure of their sensitivity, and to validate the numerical predictions of the model discussed in chapter 4. Later experiments were conducted with a variety of bacteria, including *Shewanella oneidensis*, *Clostridium acetobutylicom*, *Pseudomonas aeruginosa*, and four different strains of *Escherichia coli*. All of the results indicate that trapping occurs at significantly lower average fields than has been reported in previous work [45, 72]. In additional, several very interesting effects regarding agglomeration were observed.

5.2 Materials and Methods

In order to assess the performance of the 3DiDEP devices, they were first tested with inorganic particles. 10 μm FluoSpheres polystyrene microspheres were purchased from Invitrogen. The particles were diluted to 3.6×10^5 particles per mL, and then

spun down at 10,000 rpm for three minutes before being resuspended in buffer. A buffer of 975 μM potassium chloride, titrated to pH = 7.0 with potassium hydroxide, was chosen in order to minimize Joule heating effects and to ensure a reproducible environment. Medium conductivity was measured to be 100 μS/cm using a PC 510 pH and conductivity meter from Oakton Instruments.

A similar procedure was used for the experiments involving bacteria, except in this case, the bacteria were taken from active cultures during late log phase growth. SYBR Green or DAPI nucleic acid stains, both made by Invitrogen, were added according to the manufacturer's instructions in order to perform epifluorescence microscopy on the bacteria, which are otherwise to small to image with the 10x/0.30 objective used in this work. The bacterial cultures were kindly provided by Professors Korneel Rabaey and Phil Hugenholtz of the University of Queensland, and were grown using standard media and conditions for the respective species. *Shewanella oneidensis* strain MR1 cultures were grown under anaerobic conditions in Luria-Bertani medium at 37°C with fumarate as the terminal electron acceptor and lactate as supplemental electron donor [97]. *Pseudomonas aeruginosa* PAO1 cultures were grown in Trypticase soy agar medium at 37°C [34]. *Clostridium acetobutylicom* was cultured anaerobically in reinforced Clostridial broth supplemented with glucose at 37°C [92]. *Escherichia coli* strains K12, ABU, UTI89, and CFTO73 were all grown aerobically in Luria-Bertani medium at at 37°C [100].

As discussed in chapter 4, constant electroosmotic mobility is essential to generating reproducible results. In order to generate a consistent surface charge on the channel walls, a conditioning process was performed before all experiments. First, the channel was flushed with 10 mL of 100 mM potassium hydroxide at a rate of 0.5 mL per minute using a syringe pump. This process was repeated with deionized water, and then with suspending media. At the end of this process, care was taken to ensure that no bubbles were present in the channels, and then excess buffer was removed from the reservoirs and replaced with suspended microparticles.

5.3 Experimental Procedures

The chip was secured to the stage of a Nikon Ti inverted epifluorescence microscope, and platinum wire electrodes were inserted into the reservoirs. The electrodes were connected to a HVS448-3000D computer-controlled high voltage DC power supply made by Labsmith of Livermore, CA. Care was taken to ensure that there was no pressure or surface tension driven flow prior to beginning the experiments by equalizing the amount of fluid in each of the two reservoirs. Time lapse image sequences were collected using a CoolSNAP HQ^2 cooled CCD camera made by Photometrics of Tucson, AZ, controlled by Micro-Manager microscope control software. The complete system is shown in figure 5-1.

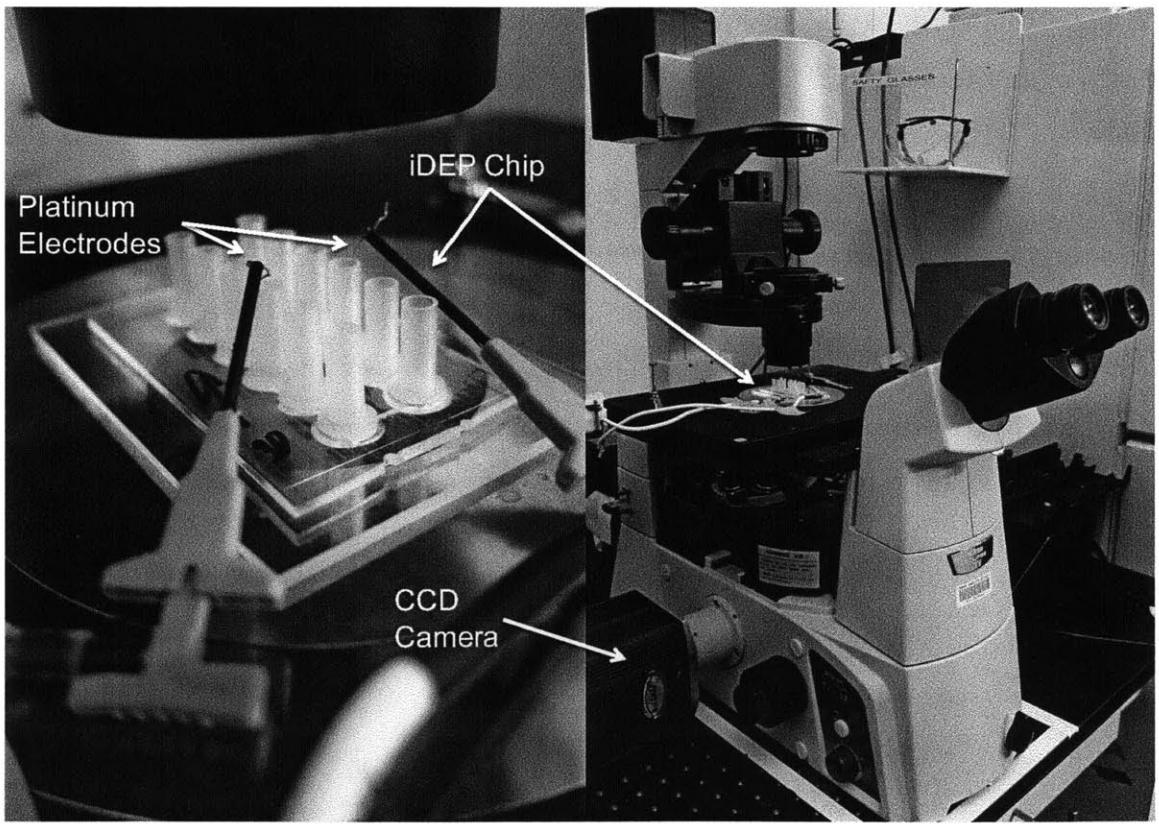

Figure 5-1: Apparatus for running DEP experiments

5.4 Model Validation with Microparticles

Polystyrene beads are commonly used to study dielectrophoresis (DEP) [72]. Their high monodispersity, homogeneous dielectric properties, and excellent suspension stability make them ideal test particles in systems that employ DEP. Although the ultimate purpose of the 3DiDEP device is to study particles with unknown dielectric properties, the purpose of the experiments with polystyrene microspheres was to validate the predictions of the numerical model.

Devices and suspensions were prepared as described in section 5.2, and a sequence of images of the microparticles were taken as they travelled through the constriction area of the channel. Since the microspheres were almost perfect insulators compared to the surrounding media, the Clausius-Mossotti factor for the experiments was - 0.5, resulting in negative DEP. The experiments were repeated at several applied voltages for both the two and three-dimensional devices. Figure 5-2 displays a time-lapse of the particles as they travelled through the 2DiDEP channel, with numerically predicted particle streamlines overlaid over the upper half of the channel. At voltages below 75 volts, no trapping was observed, but particle trajectories clearly demonstrate that the microspheres experienced a focusing effect, as predicted by the numerical model in chapter 4. At voltages in excess of 75 volts, particle motion due to DEP was greater than particle motion due to electrophoresis and electroosmosis, and particles trapped upstream of the constriction.

When these experiments were repeated in the 3DiDEP device, much lower applied voltages were required to achieve trapping. In fact, for 10 μm beads, trapping rather than focusing was observed for potentials as low as three volts. Figure 5-3 shows time lapse images for the beads over a range of potentials. In all cases, complete trapping was observed. Numerically predicted trapping zones and particle streamlines are overlaid. The trapping zones do not match exactly between experiment and simulation due to small variations in the electrophoretic mobility of the beads.

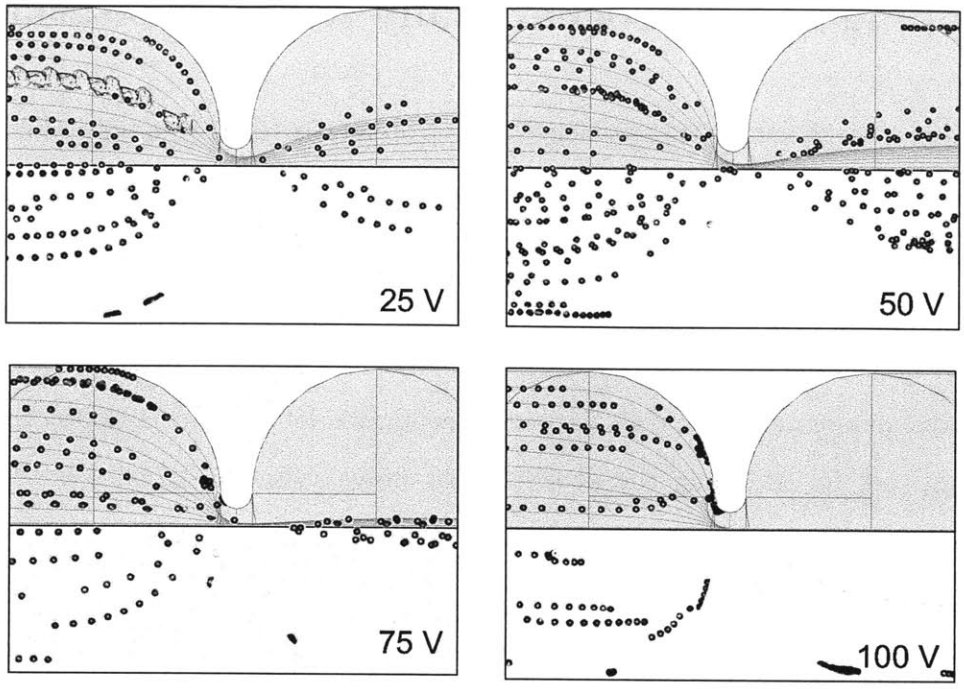

Figure 5-2: Focusing and trapping of 10 μm polystyrene beads experiencing negative DEP in a 2DiDEP channel. Predicted particle streamlines and trapping zones are overlaid

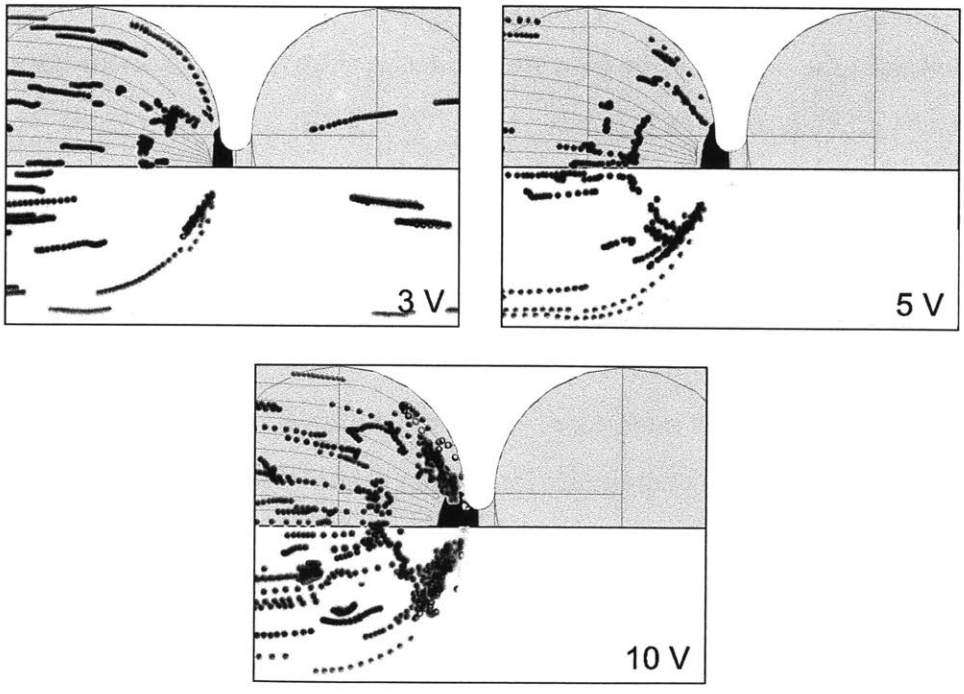

Figure 5-3: Focusing and trapping of 10 μm polystyrene beads experiencing negative DEP in a 3DiDEP channel. Predicted particle streamlines (red lines) and trapping zones (black) are overlaid

5.5 Trapping of Electrochemically Active Bacteria

As discussed in chapter 2, DC insulator-based dielectrophoresis (iDEP) is unique in that the polarizability of the particles under test is almost exclusively a function of the particles surface properties. This capability is of particular interest when electrochemically active bacteria are considered. For example, *Shewanella oneidensis* strain MR1 is known to be capable of extracellular electron transfer due to the unique capabilities of bacterial nanowires located in the outer membrane [30]. iDEP is therefore a very promising tool for studying the properties of these bacteria. In this work, *S. oneidensis* strain MR1 was cultured anaerobically, stained with DAPI, and suspended in low conductivity buffer as described in section 5.2. Times lapse images were taken using a Zeiss Axioplan laser scanning confocal microscope. Figure 5-4 shows observed trapping of *S. oneidensis* in a 3DiDEP channel at 25 and 50 volts. The electrophoretic mobility of the bacteria is greater than the electroosmotic mobility of the channel, so the bacteria move upwards towards the positively biased electrode. Positive DEP is observed in both cases, with significantly stronger trapping observed in the higher voltage case. This result provides evidence that the outer membrane surface conductivity of this bacteria is greater than 100 μS/cm.

In order to provide a comparison to the results observed for *S.oneidensis*, the experiments were repeated with *Clostridium acetobutylicum*. Unlike *S. oneidensis*, *C. acetobutylicum* are a gram positive species, and therefore have a thicker peptidoglycan layer in place of an outer membrane [59]. Their ability to synthesize commercially valuable long chain hydrocarbons such as acetone and butanol has garnered them significant attention as a promising candidate for biofuel production, and makes them a species of interest in their own right for DEP studies [37].

Figure 5-5 shows observed trapping of *C. acetobutylicum* in a 3DiDEP channel at applied voltages of 25 and 50 V. Unlike the case of *S. oneidensis*, where positive trapping of bacteria was very clearly the dominant behavior, *C. acetobutylicum* exhibited more ambiguous behavior. Clearly, a large portion of bacteria passed through the channel, with a focusing effect due to incomplete trapping. In addition, there

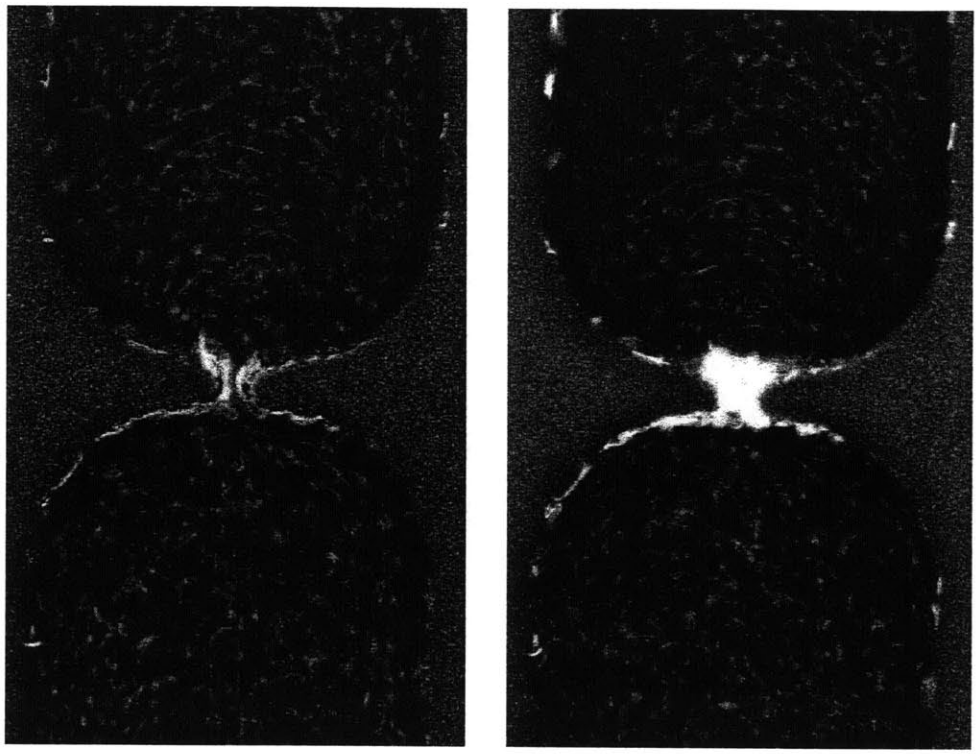

Figure 5-4: Trapping of *Shewanella oneidensis* strain MR1 in a 3DiDEP channel at 25 V and 50 V

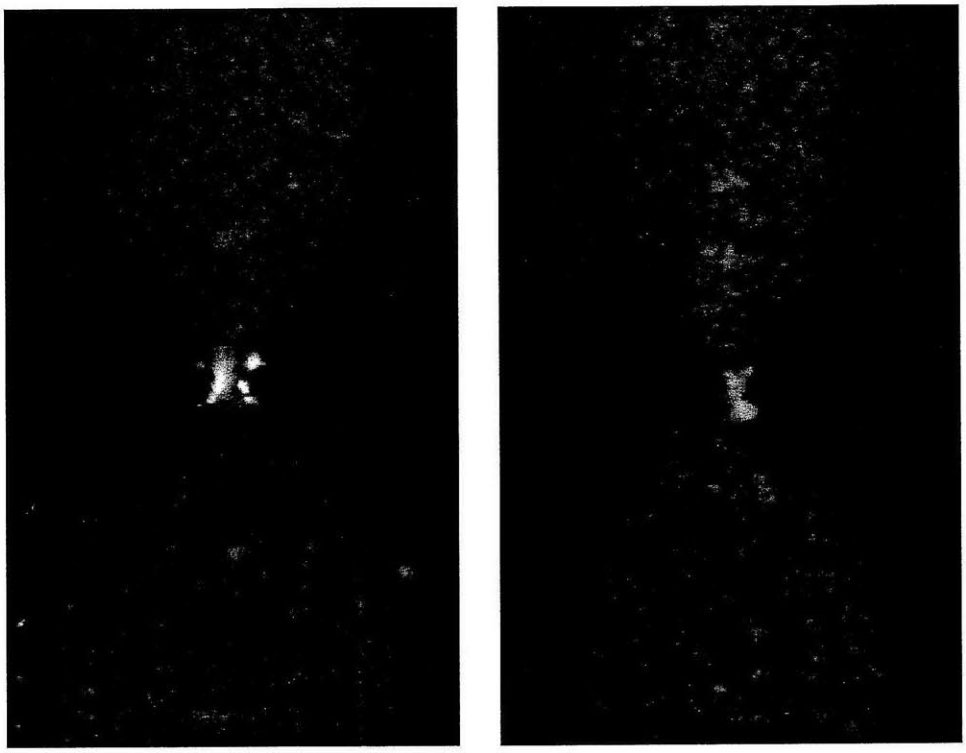

Figure 5-5: Trapping and focusing of *Clostridium acetobutylicum* in a 3DiDEP channel at 25 V and 50 V

weak trapping of bacteria around the constriction at 25 V, but it did not appear to get stronger when the voltage is increased to 50 V. One possible explanation for this behavior is that because *C. acetobutylicum* are able to form spores, which might have very different surface properties, the bacteria and spores might trap differently. In this experiment, the 50 V data was collected immediately following the 25 V data, so it is possible that the population distribution was unsteady during this time. If this was the case, the 50 V experiment is probing a different ensemble of organisms than the 25 V experiment, which would explain the change in trapping in trapping behavior.

Another interesting observation regarding these experiments was made at their completion. It was observed that the highly concentrated regions of *S. oneidensis* visible in figure 5-4 remained intact, even after the applied potential was turned off, while the *C. acetobutylicum* rapidly dispersed. Complete coverage of electrodes with biofilms in microbial electrochemical devices is a constant challenge in the field today, so the ability to to produce agglomerates of electrochemically active bacteria is of particular interest. Recently, work has been done in which *Pseudomonas aeruginosa* strain PA14 was observed to form biofilm streamers in high shear rate laminar flow [86]. However, this effect was observed on the order of hours, whereas the agglomerates observed here formed in less than a minute. The exact physics and biology of the formation mechanism are unknown, but the interspecies variation observed here suggests that the surface properties of the bacteria play a large role.

5.6 Agglomeration Potential of *Pseudomonas aeruginosa*

The stark differences in behavior of *S. oneidensis* and *C. acetobutylicum* in terms of both DEP trapping and agglomeration formation were striking, but with only two species tested, it was impossible to speculate about whether the variations were due to the gram positive gram negative difference, or whether it was due to the unique

membrane properties of *S. oneidensis*. *Pseudomonas aeruginosa* PAO1 was selected in order to provide further information. Like *S. oneidensis*, it is gram negative, but it does not have the same unique electrochemical properties. Tests were conducted using the same materials and procedures as described previously. Figure 5-6 shows a time lapse series of images of *P. aeruginosa* in a 3DiDEP channel with an applied voltage of 25 V. In the first image, the voltage was on, and the bacteria had reached a steady state, with incomplete positive DEP trapping clearly visible on the right side of the image. The voltage was turned off immediately afterwards, and the bacteria could be seen to rapidly disperse, with near complete dispersal within three seconds.

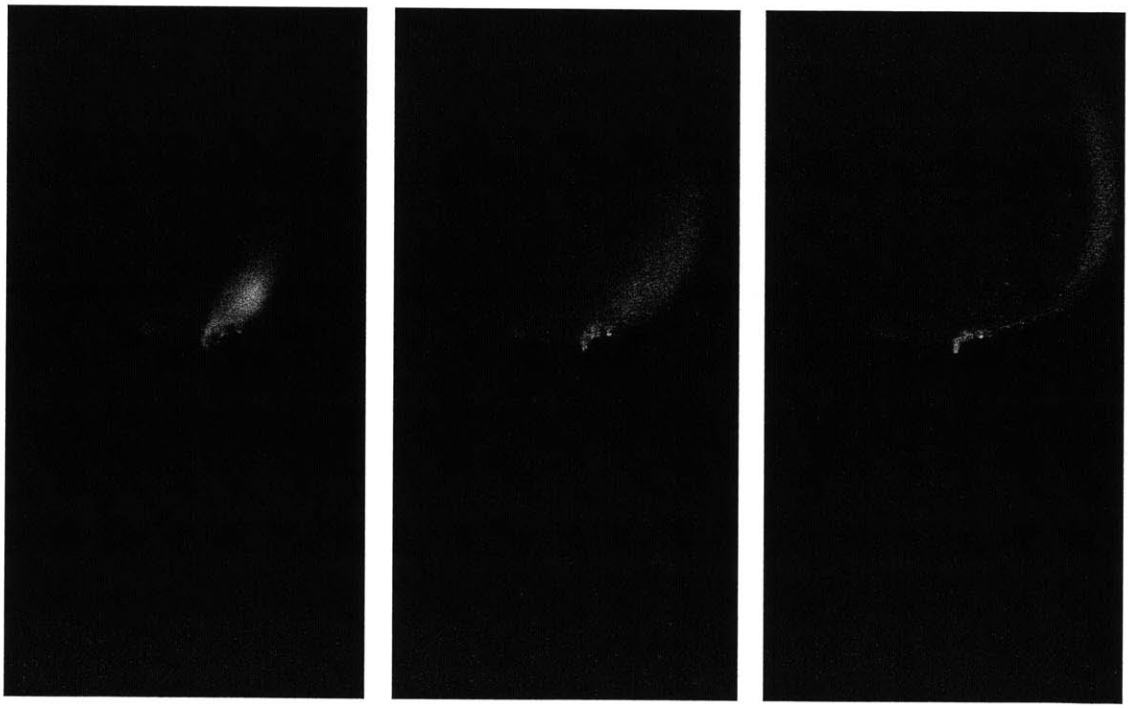

Figure 5-6: Time sequence at one frame per second of *Clostridium acetobutylicum* trapping in a 3DiDEP channel after 25 V across the channel was removed

Compared to the results for *S. oneidensis* and *C. acetobutylicum*, *P. aeruginosa* exhibited an interesting hybrid behavior. It demonstrated strong positive dielectrophoresis like *S. oneidensis*, suggesting a relatively conductive outer membrane, but unlike *S. oneidensis*, it did not form an agglomerate. This was particularly surprising given *P. aeruginosa's* well documented propensity for biofilm formation [23].

One possible hypothesis for this observation was that PAO1, the strain studied here, is only a mildly opportunistic pathogen. Since biofilm formation has been identified as a key component of pathogenicity [21, 20], more hazardous strains such as PA14 or others observed clinically might exhibit a higher propensity to agglomerate.

5.7 Intraspecies Membrane Property Variations in Pathogenic *Escherichia coli*

The suggestive results from the investigation of *P. aeruginosa* motivated further study of the link between pathogenicity and agglomerate formation. *Escherichia coli*, an extremely common gram negative bacteria with many well characterized pathogenic and nonpathogenic strains, present an ideal test case for this hypothesis [15]. In particular, *E. coli* account for roughly 80% of all urinary tract infections [93], which are a common and potentially dangerous problem in hospitals. A number of techniques are currently being developed to identify the individual strains involved; one of the most promising uses microarray analysis and comparative genomics to identify specific strains [96]. Although effective, this process require the facilities of a full lab, and is not easily scalable to clinical environments. If a low cost device such as the 3DiDEP system presented here were able to select for pathogenicity, it could be of significant value.

To determine whether the 3DiDEP device was capable of resolving pathogenic from nonpathogenic bacteria, three pathogenic strains of *E. coli* were tested against *E. coli* K12, a commonly used non-pathogenic lab strain. Asymptomatic bacteriuria ABU, reference strain CFT073, and cystitis strain UTI89 were all isolated from clinical patients, and were cultured in the lab of Professor Mark Schembri at the University of Queensland. The strains were tested in the same manner as the previous experiments, as described in section 5.2. In all cases, the samples were loaded into 3DiDEP channels, and a voltage of 25 V was applied across the channel for forty seconds before being turned off. Figure 5-7 shows images of trapped pathogenic *E.*

coli in the channels during the experiment and then ten seconds after the field was turned off. Positive DEP trapping was observed for all three strains. Interestingly, the asymptomatic ABU appeared to trap slightly less robustly than the other two, but further experiments are needed to verify this observation. Agglomeration of bacteria was also observed in all three cases, though in the case of UTI89, the agglomerate detached from the constriction and moved down the channel in a single piece, as shown in figure 5-7.

Control experiments were performed with *E. coli* K12. First, the procedure used to trap the pathogenic strains was employed, but at 25 volts applied across the channel, no trapping was observed. Given that K12 is the same size as the pathogenic strains, this result implies that the outer membrane of the K12 was measurably less conductive than that of the pathogenic strains. The experiment was then repeated at 100 volts. Although the increased voltage was sufficient to induce positive DEP, after the voltage was turned off, the bacteria rapidly dispersed, confirming that no agglomeration occurred. Figure 5-8 demonstrates the trapping and agglomeration behavior of *E. coli* K12. To the author's knowledge, this result represents the first ever observation of intraspecies variation of membrane surface properties using iDEP.

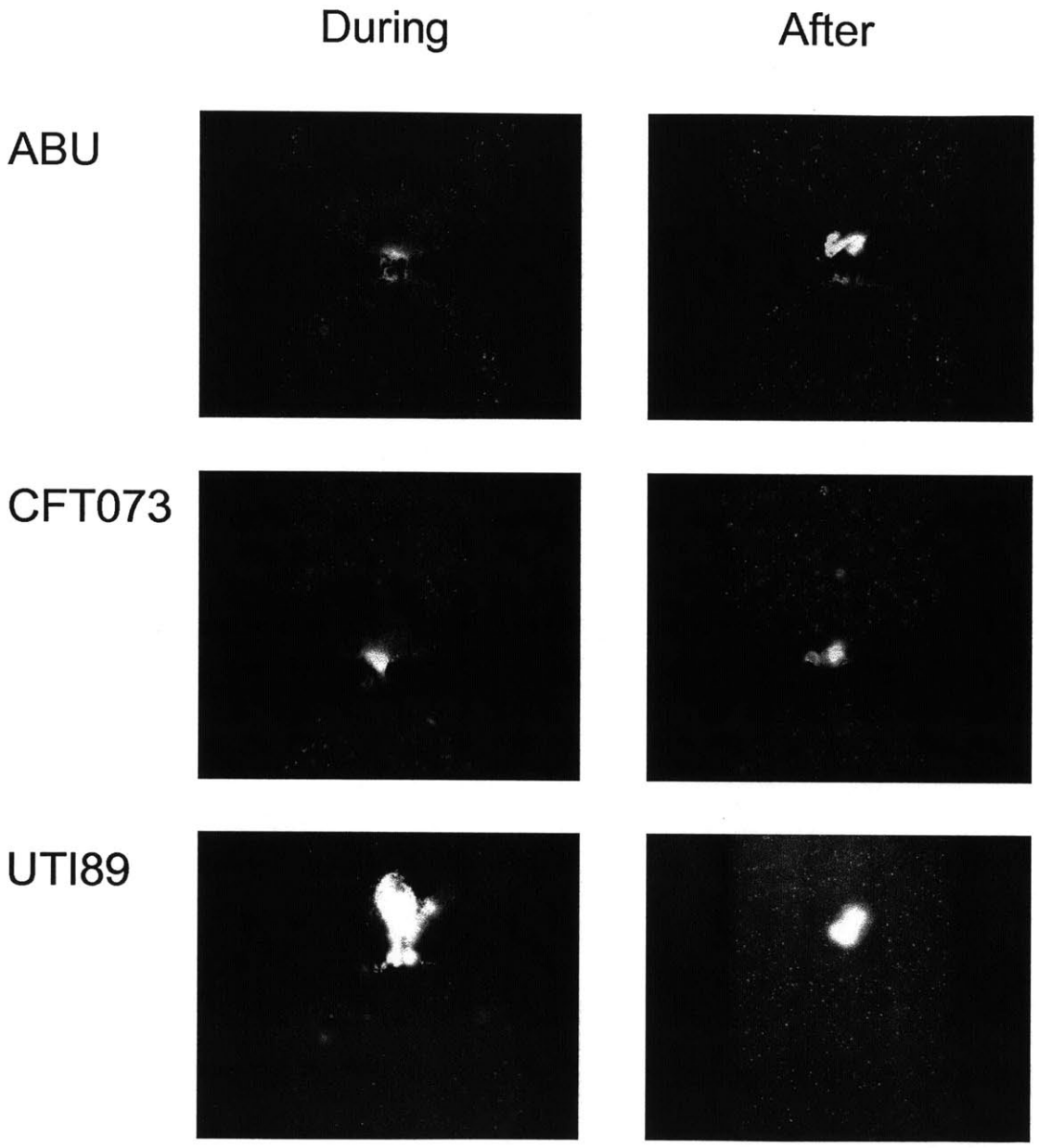

Figure 5-7: *Echerichia coli* strains (from top) ABU, CFT073, and UTI89 during (left) and immediately after (right) trapping using 25 V in a 3DiDEP channel

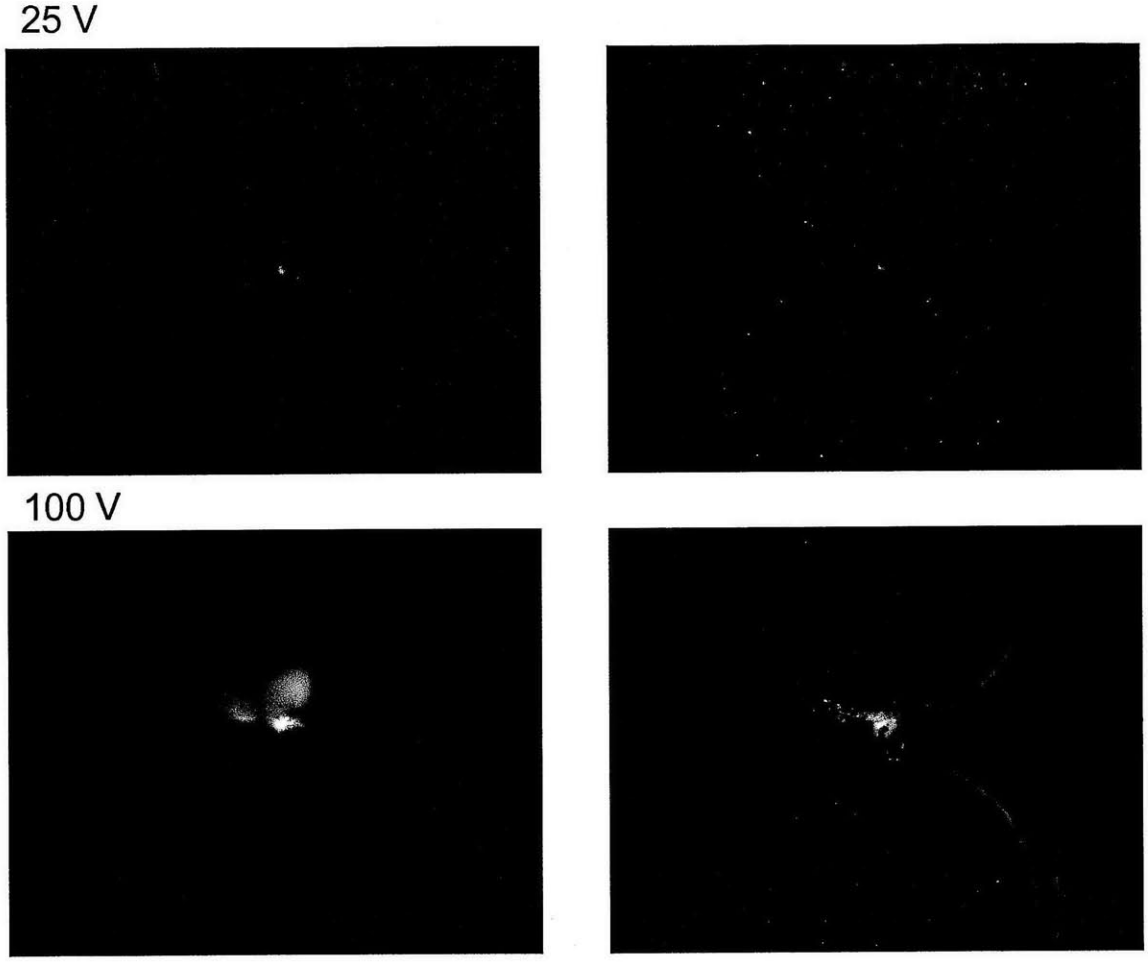

Figure 5-8: *Echerichia coli* strain K12 during (left) and immediately after (right) trapping using an applied potential of 25 V (top) and 100 V (bottom) in a 3DiDEP channel

Chapter 6

Conclusions and Future Work

6.1 Summary of Results

In this work, a novel technique is employed to fabricate microfluidic devices that harness the physics of three-dimensional insulator-based dielectrophoresis (3DiDEP) to trap and focus microparticles. These systems use large constriction ratios to generate larger dielectrophoretic forces than traditional two-dimensional designs, which allows for trapping of smaller and more sensitive microparticles, such as bacteria, with minimal temperature variations within the device. In chapters 4 and 5, it was shown that by constricting an insulator-based dielectrophoresis (iDEP) channel in two dimensions rather than one, significantly stronger trapping forces could be generated for the same variation in temperature within the channel. For small particles such as bacteria, this increase in sensitivity could mean the difference between thermally lysing a culture and being able to recover viable samples for future study at the end of an experiment.

One of the major challenges in the field of iDEP has been the commercialization of the technology. Despite eight years of development, iDEP devices have yet to find a commercially viable application. In part, this is due to the technical limitations of existing chips. Devices made from borosilicate glass would be prohibitively expensive, and standard PDMS devices require cleanroom procedures and slow batch-mode curing that would make large scale production difficult. The novel micromachining

Table 6.1: Trapping of micron-sized particles and live cells using iDEP

Year	Author	Reference	Trapping field (V/mm)
2003	Cummings	[22]	100
2004	Lapizco-Encinas	[45]	18
2005	Barrett	[4]	30
2007	Pysher	[77]	20
2009	Cho	[19]	128
2009	Baylon-Cardiel	[5]	75
2010	Chen	[17]	20
2010	Moncada-Hernández	[63]	40
2010	Staton	[94]	15
2011	*This work*		2.5

fabrication technique developed in this work addresses these challenges by using traditional three-axis CNC milling to generate microfluidic chips out of low cost plastic sheet. This technique is also advantageous in that it allows for easy fabrication of three-dimensional features in the device with little or no increase in fabrication time.

The increased sensitivity of the 3DiDEP device allowed for trapping of bacteria at 2.5 V/mm, which is nearly an order of magnitude lower than applied fields used in previous works, as shown in table 6.1. According to our numerical model, the conditions of the experiment generated a maximum temperature variation of 0.65°C, ensuring that the bacteria were not damaged or affected by Joule heating effects.

Furthermore, the higher sensitivity of the 3DiDEP device presented here resulted in small changes in particle polarizability, producing large changes in trapping behavior. The enhanced sensitivity inherent to the device was applied to observe differences in the dielectric properties of the membranes of *Shewanella oneidensis* strain MR1, *Clostridium acetobutylicum*, *Pseudomonas aeruginosa* strain PAO1, and four different strains of *Escherichia coli*. In particular, preliminary results have demonstrated differences in trapping behavior between gram negative and gram positive bacteria, and have also observed a correlation between the unique functional properties of the bacteria and its potential for the formation of agglomerates when exposed to large electric field intensity gradients. In particular, in a study of three different pathogenic

and one nonpathogenic strain of *E. coli*, a clear correlation was observed between the pathogenicity of the bacteria and both the membrane conductivity and the agglomeration formation potential. Previous works have demonstrated interspecies, live-dead, and size-based sorting using iDEP devices [45, 44, 94]. However, this work represents the first observation of intraspecies differences in membrane surface properties using iDEP.

6.2 Opportunities for Future Work

In this work, a novel three-dimensional microfluidic device was designed, fabricated, modeled, and then applied to study the dielectric properties of bacterial membranes. The results presented in chapter 5 demonstrate several significant differences in outer membrane structures of bacteria, but a great deal of work remains to be done to fully understand some of the observed behaviors.

Anaerobically cultured *S. oneidensis* strain MR1 have been shown to exhibit positive dielectrophoresis at low applied fields in weakly conductive buffer, and that the bacteria have a tendency to agglomerate when exposed to large electric field intensity gradients. *S. oneidensis* are known for their ability to respire anaerobically via extracellular electron transfer using an electrode or other insoluble electron acceptor, and it was hypothesized that the unique membrane proteins required to perform this function could have a significant impact on the dielectric and mechanical properties of the outer membrane of the bacteria. In order to verify this hypothesis, it would be very interesting to compare the trapping behavior of *S. oneidensis* grown under different conditions. Bacteria grown aerobically, anaerobically with soluble electron acceptors, anaerobically with insoluble acceptors, and anaerobically in a bioelectrochemical systems might all be expected to exhibit different membrane polarizability and agglomeration characteristics. It would also be of value to perform similar experiments on another extracellular electron transfer organism, *Geobacter sulfurreducens*. *G. sulfurreducens* is an obligate anaerobe that is unique in its inability to synthesize mediators to serve as electron shuttles. As a result, it requires a direct electrical

connection with its insoluble electron acceptor. These characteristics might result in unique membrane dielectric properties since the bacteria rely exclusively on their outer membrane proteins for respiration.

The observation of intraspecies variation of membrane properties between four strains *E. coli* is a measurable achievement in the field of iDEP. The apparent correlation between the membrane polarizability and agglomeration potential and the pathogenicity of the strain raises the possibility of a low-cost rapid clinical diagnostic tool for testing patients suffering from certain diseases. Further testing on a much wider range of *E. coli* strains is needed before any firm conclusions are drawn. Additionally, since biofilms play a large role in infections caused by wide range of bacteria, including numerous strains of *P. aeruginosa* and *E. coli* as well as *Staphylococcus epidermidis* and *Staphylococcus aureus* [21], the number of pathogenic strains of bacteria that could be detected using the 3DiDEP devices might be very large. In additional to its utility as a clinical tool, such studies could also provide valuable insight into the formation mechanisms of biofilms in pathogenic bacteria.

Lastly, the vast majority of studies that use iDEP presently stop at the imaging stage, and do not attempt to apply the separation to any particular process. The utility of all of the studies outlined above would be greatly enhanced if it were possible to extract the trapped bacteria from the device at the end of the experiment. If genetic or phenotypic variations in the trapped bacteria compared to the original culture were observed, that information could be used to further existing knowledge about the nature of biofilm-forming bacteria.

Appendix A

Machine Code for 3DiDEP Device

(PROGRAM NAME - 3DiDEP_Channels v5)

T1 M06

G120 B1 H1

G123 H1 W1 X2 Y0

M05

G0 Z40

N1(62.5 mil End Mill - D0 H1)

T1 M06

G120 B1 H1

G54

G43 H1

S48000 M03

M8

M0

G0 Z1

G0 X-29 Y-15

G1 Z0 F600

X29

Y-13.73

X-29

Y-12.46

X29

Y-11.19

X-29

Y-9.92

X29

Y-8.65

X-29

Y-7.38

X29

Y-6.11

X-29

Y-4.84

X29

Y-3.57

X-29

Y-2.3

X29

Y-1.03

X-29

Y0.24

X29

Y1.51

X-29

Y2.78

X29

Y4.05

X-29

Y5.32

X29

Y6.59

X-29

Y7.86

X29

Y9.13

X-29

Y10.4

X29

Y11.67

X-29

Y12.94

X29

Y14.21

X-29

Y15.48

X29

Z1

G0 Z1

G0 X-21 Y5

G1 Z-1.5 F75

Z1

G0 X-21 Y-5

G1 Z-1.5 F75

Z1

G0 X-14 Y5

G1 Z-1.5 F75

Z1

G0 X-14 Y-5
G1 Z-1.5 F75
Z1

G0 X-7 Y5
G1 Z-1.6 F75
Z1
G0 X-7 Y-5
G1 Z-1.6 F75
Z1

G0 X0 Y5
G1 Z-1.6 F75
Z1
G0 X0 Y-5
G1 Z-1.6 F75
Z1

G0 X7 Y5
G1 Z-1.6 F75
Z1
G0 X7 Y-5
G1 Z-1.6 F75
Z1

G0 X14 Y5
G1 Z-1.6 F75
Z1
G0 X14 Y-5
G1 Z-1.6 F75

```
Z1

G0 X21 Y5
G1 Z-1.6 F75
Z1
G0 X21 Y-5
G1 Z-1.6 F75
Z1

G0 Z70
G0 X0 Y0
M5
M09

N1(15 mil End Mill - D0 H1)
T1 M06
G120 B1 H1
G54
G43 H1
S48000 M03
M8
M0

G00 X-21.0395 Y4.9
G0 Z1
G1 Z-.49 F200.
Y.2355
X-20.9605
Y4.9895
X-21.0395
```

Z1.

G0 X-20.9605 Y-4.9895

G1 Z-.49

Y-.2355

X-21.0395

Y-4.9895

X-20.9605

Z1.

G0 X-21.0595 Y5.

G1 Z-.5 F50

Y.225

G3 X-21.05 Y.2155 I.0095 J0.

G1 X-20.95

G3 X-20.9405 Y.225 I0. J.0095

G1 Y5.

G3 X-20.95 Y5.0095 I-.0095 J0.

G1 X-21.05

G3 X-21.0595 Y5. I0. J-.0095

G1 Z1.

G0 X-20.9405 Y-5.

G1 Z-.5

Y-.225

G3 X-20.95 Y-.2155 I-.0095 J0.

G1 X-21.05

G3 X-21.0595 Y-.225 I0. J-.0095

G1 Y-5.

G3 X-21.05 Y-5.0095 I.0095 J0.

G1 X-20.95

G3 X-20.9405 Y-5. I0. J.0095

G1 Z1.

G00 X-14.0395 Y4.9

G1 Z-.49 F200.

Y.2355

X-13.9605

Y4.9895

X-14.0395

Z1.

G0 X-13.9605 Y-4.9895

G1 Z-.49

Y-.2355

X-14.0395

Y-4.9895

X-13.9605

Z1.

G0 X-14.0595 Y5.

G1 Z-.5 F50.

Y.225

G3 X-14.05 Y.2155 I.0095 J0.

G1 X-13.95

G3 X-13.9405 Y.225 I0. J.0095

G1 Y5.

G3 X-13.95 Y5.0095 I-.0095 J0.

G1 X-14.05

G3 X-14.0595 Y5. I0. J-.0095

G1 Z1.

G0 X-13.9405 Y-5.

G1 Z-.5

Y-.225

G3 X-13.95 Y-.2155 I-.0095 J0.

G1 X-14.05

G3 X-14.0595 Y-.225 I0. J-.0095

G1 Y-5.

G3 X-14.05 Y-5.0095 I.0095 J0.

G1 X-13.95

G3 X-13.9405 Y-5. I0. J.0095

G1 Z1.

G00 X-7.0395 Y4.9

G0 Z1

G1 Z-.49 F200.

Y.2355

X-6.9605

Y4.9895

X-7.0395

Z1.

G0 X-6.9605 Y-4.9895

G1 Z-.49

Y-.2355

X-7.0395

Y-4.9895

X-6.9605

Z1.

G0 X-7.0595 Y5.

G1 Z-.5 F50.

Y.225

G3 X-7.05 Y.2155 I.0095 J0.

G1 X-6.95

G3 X-6.9405 Y.225 I0. J.0095

G1 Y5.

G3 X-6.95 Y5.0095 I-.0095 J0.

G1 X-7.05

G3 X-7.0595 Y5. I0. J-.0095

G1 Z1.

G0 X-6.9405 Y-5.

G1 Z-.5

Y-.225

G3 X-6.95 Y-.2155 I-.0095 J0.

G1 X-7.05

G3 X-7.0595 Y-.225 I0. J-.0095

G1 Y-5.

G3 X-7.05 Y-5.0095 I.0095 J0.

G1 X-6.95

G3 X-6.9405 Y-5. I0. J.0095

G1 Z1.

G00 X-.0395 Y4.9

G1 Z-.49 F200.

Y.2355

X.0395

Y4.9895

X-.0395

Z1.

G0 X.0395 Y-4.9895

G1 Z-.49

Y-.2355

X-.0395

Y-4.9895

X.0395

Z1.

G0 X-.0595 Y5.

G1 Z-.5 F50.

Y.225

G3 X-.05 Y.2155 I.0095 J0.

G1 X.05

G3 X.0595 Y.225 I0. J.0095

G1 Y5.

G3 X.05 Y5.0095 I-.0095 J0. G1 X-.05 G3 X-.0595 Y5. I0. J-.0095

G1 Z1.

G0 X.0595 Y-5.

G1 Z-.5

Y-.225

G3 X.05 Y-.2155 I-.0095 J0.

G1 X-.05

G3 X-.0595 Y-.225 I0. J-.0095

G1 Y-5.

G3 X-.05 Y-5.0095 I.0095 J0.

G1 X.05

G3 X.0595 Y-5. I0. J.0095

G1 Z1.

G00 X6.9605 Y4.9

G1 Z-.49 F200.

Y.2355

X7.0395

Y4.9895

X6.9605

Z1.

G0 X7.0395 Y-4.9895

G1 Z-.49

Y-.2355

X6.9605

Y-4.9895

X6.9605

Z1.

G0 X6.9405 Y5.

G1 Z-.5 F50.

Y.225

G3 X6.95 Y.2155 I.0095 J0.

G1 X7.05

G3 X7.0595 Y.225 I0. J.0095

G1 Y5.

G3 X7.05 Y5.0095 I-.0095 J0.

G1 X6.95

G3 X6.9405 Y5. I0. J-.0095

G1 Z1.

G0 X7.0595 Y-5.

G1 Z-.5

Y-.225

G3 X7.05 Y-.2155 I-.0095 J0.

G1 X6.95

G3 X6.9405 Y-.225 I0. J-.0095

G1 Y-5.

G3 X6.95 Y-5.0095 I.0095 J0.

G1 X7.05

G3 X7.0595 Y-5. I0. J.0095

G1 Z1.

G00 X13.9605 Y4.9

G1 Z-.49 F200.

Y.2355

X14.0395

Y4.9895

X13.9605

Z1.

G0 X14.0395 Y-4.9895

G1 Z-.49

Y-.2355

X13.9605

Y-4.9895

X13.9605

Z1.

G0 X13.9405 Y5.

G1 Z-.5 F50.

Y.225

G3 X13.95 Y.2155 I.0095 J0.

G1 X14.05

G3 X14.0595 Y.225 I0. J.0095

G1 Y5.

G3 X14.05 Y5.0095 I-.0095 J0.

G1 X13.95

G3 X13.9405 Y5. I0. J-.0095

G1 Z1.

G0 X14.0595 Y-5.

G1 Z-.5

Y-.225

G3 X14.05 Y-.2155 I-.0095 J0.

G1 X13.95

G3 X13.9405 Y-.225 I0. J-.0095

G1 Y-5.

G3 X13.95 Y-5.0095 I.0095 J0.

G1 X14.05

G3 X14.0595 Y-5. I0. J.0095

G1 Z1.

G00 X20.9605 Y4.9

G1 Z-.49 F200.

Y.2355

X21.0395

Y4.9895

X20.9605

Z1.

G0 X21.0395 Y-4.9895

G1 Z-.49

Y-.2355

X20.9605

Y-4.9895

X20.9605

Z1.

G0 X20.9405 Y5.

G1 Z-.5 F50.

Y.225

G3 X20.95 Y.2155 I.0095 J0.

G1 X21.05

G3 X21.0595 Y.225 I0. J.0095

G1 Y5.

G3 X21.05 Y5.0095 I-.0095 J0.

G1 X20.95

G3 X20.9405 Y5. I0. J-.0095

G1 Z1.

G0 X21.0595 Y-5.

G1 Z-.5

Y-.225

G3 X21.05 Y-.2155 I-.0095 J0.

G1 X20.95

G3 X20.9405 Y-.225 I0. J-.0095

G1 Y-5.

G3 X20.95 Y-5.0095 I.0095 J0.

G1 X21.05

G3 X21.0595 Y-5. I0. J.0095

G1 Z1.

G0 Z70

G0 X0 Y0

M5

M09

N1(2 mil End Mill - D0 H1)

T1 M06

G120 B1 H1

G54

G43 H1

S48000 M03

M8

M0

G0 Z1

G0 X-21.052 Y-.052

Z-.015 F10

G3 X-21.052 Y.052 I0 J.052

G1 Z1

X-20.948 Y-.052

Z-.015

G2 X-20.948 Y.052 I0 J.052

G1 Z1

G0 X-14.052 Y-.052

G1 Z-.015 F10

G3 X-14.052 Y.052 I0 J.052

G1 Z1

X-13.948 Y-.052

Z-.015

G2 X-13.948 Y.052 I0 J.052

G1 Z1

G0 X-7.052 Y-.052

G1 Z-.015 F10

G3 X-7.052 Y.052 I0 J.052

G1 Z1

X-6.948 Y-.052

Z-.015

G2 X-6.948 Y.052 I0 J.052

G1 Z1

G0 X-.052 Y-.052

G1 Z-.015 F10

G3 X-.052 Y.052 I0 J.052

G1 Z1

X.052 Y-.052

Z-.015

G2 X.052 Y.052 I0 J.052

G1 Z1

G0 X6.948 Y-.052

G1 Z-.015 F10

G3 X6.948 Y.052 I0 J.052

G1 Z1

X7.052 Y-.052

Z-.015

G2 X7.052 Y.052 I0 J.052

G1 Z1

G0 X13.948 Y-.052

G1 Z-.015 F10

G3 X13.948 Y.052 I0 J.052

G1 Z1

X14.052 Y-.052

Z-.015

G2 X14.052 Y.052 I0 J.052

G1 Z1

G0 X20.948 Y-.052

G1 Z-.015 F10

G3 X20.948 Y.052 I0 J.052

G1 Z1

X21.052 Y-.052

Z-.015

G2 X21.052 Y.052 I0 J.052

G1 Z1

G0 Z70.

G0 X0 Y0

M5

M09

M30

Bibliography

[1] Y. Ai, S. W. Joo, S. Liu, and S. Qian. Direct Numerical Simulation of Particle Separation by Direct Current Dielectrophoresis. *Proceedings of ASME NMHMT*, 1:1–6, 2009.

[2] S. Allison. Electrophoretic mobility and primary electroviscous effect of dilute "hard" prolate ellipsoids. *Journal of Colloid and Interface Science*, 282(1):231–237, 2005.

[3] D. Anderson and M. Leach. Harvesting and redistributing renewable energy: on the role of gas and electricity grids to overcome intermittency through the generation and storage of hydrogen. *Energy Policy*, 32(14):1603–1614, 2004.

[4] L. M. Barrett, A. J. Skulan, A. K. Singh, E. B. Cummings, and G. J. Fiechtner. Dielectrophoretic manipulation of particles and cells using insulating ridges in faceted prism microchannels. *Analytical Chemistry*, 77(21):6798–6804, 2005.

[5] J. L. Baylon-Cardiel, B. H. Lapizco-Encinas, C. Reyes-Betanzo, A. V. Chavez-Santoscoy, and S. O. Martinez-Chapa. Prediction of trapping zones in an insulator-based dielectrophoretic device. *Lab on a Chip*, 9(20):2896–2901, 2009.

[6] D. R. Bond, D. E. Holmes, L. M. Tender, and D. R. Lovley. Electrode-reducing microorganisms that harvest energy from marine sediments. *Science*, 295(5554):483–485, 2002.

[7] D. R. Bond and D. R. Lovley. Electricity production by Geobacter sulfurreducens attached to electrodes. *Applied and Environmental Microbiology*, 69(3):1548–1555, 2003.

[8] W. A. Braff and C. R. Buie. High sensitivity three-dimensional insulator-based dielectrophoresis. 2011. (In preparation).

[9] L. Brown, T. Koerner, J. Horton, and R. Oleschuk. Fabrication and characterization of poly(methylmethacrylate) microfluidic devices bonded using surface modifications and solvents. *Lab on a Chip*, 6(1):66–73, 2006.

[10] H. Bruus. *Theoretical Microfluidics (Oxford Master Series in Physics)*. Oxford University Press, USA, 2008.

[11] J. P. Burt, R. Pethig, P. R. Gascoyne, and F. F. Becker. Dielectrophoretic characterisation of Friend murine erythroleukaemic cells as a measure of induced differentiation. *Biochimica et Biophysica acta*, 1034(1):93–101, 1990.

[12] C. S. Butler and R. Nerenberg. Performance and microbial ecology of air-cathode microbial fuel cells with layered electrode assemblies. *Applied Microbiology and Biotechnology*, 86(5):1399–1408, 2010.

[13] F. Caccavo Jr, P. C. Schamberger, K. Keiding, and P. H. Nielsen. Role of Hydrophobicity in Adhesion of the Dissimilatory Fe(III)-Reducing Bacterium Shewanella alga to Amorphous Fe(III) Oxide. *Applied and Environmental Microbiology*, 63(10):3837–3843, 1997.

[14] X. Cao, X. Huang, X. Zhang, P. Liang, and M. Fan. A mini-microbial fuel cell for voltage testing of exoelectrogenic bacteria. *Frontiers of Environmental Science and Engineering in China*, 3(3):307–312, 2009.

[15] M. Castellarnau, A. Errachid, C. Madrid, A. Juárez, and J. Samitier. Dielectrophoresis as a tool to characterize and differentiate isogenic mutants of Escherichia coli. *Biophysical Journal*, 91(10):3937–3945, 2006.

[16] S. K. Chaudhuri and D. R. Lovley. Electricity generation by direct oxidation of glucose in mediatorless microbial fuel cells. *Nature Biotechnology*, 21(10):1229–1232, 2003.

[17] D. Chen, H. Du, and C. Y. Tay. Rapid Concentration of Nanoparticles with DC Dielectrophoresis in Focused Electric Fields. *Nanoscale Research Letters*, 5(1):55–60, 2010.

[18] R. Chen, H. Guo, Y. Shen, Y. Hu, and Y. Sun. Determination of EOF of PMMA microfluidic chip by indirect laser-induced fluorescence detection. *Sensors and Actuators B-Chemical*, 114(2):1100–1107, 2006.

[19] Y.-K. Cho, S. Kim, K. Lee, C. Park, J.-G. Lee, and C. Ko. Bacteria concentration using a membrane type insulator-based dielectrophoresis in a plastic chip. *Electrophoresis*, 30(18):3153–3159, 2009.

[20] J. W. Costerton, Z. Lewandowski, D. E. Caldwell, D. R. Korber, and H. M. Lappin-Scott. Microbial biofilms. *Annual Review of Microbiology*, 49:711–745, 1995.

[21] J. W. Costerton, P. S. Stewart, and E. P. Greenberg. Bacterial biofilms: a common cause of persistent infections. *Science*, 284(5418):1318–1322, 1999.

[22] E. B. Cummings and A. Singh. Dielectrophoresis in microchips containing arrays of insulating posts: Theoretical and experimental results. *Analytical Chemistry*, 75(18):4724–4731, 2003.

[23] R. M. Donlan and J. W. Costerton. Biofilms: survival mechanisms of clinically relevant microorganisms. *Clinical Microbiology Reviews*, 15(2):167–193, 2002.

[24] A. Esteve-Nunez, J. Sosnik, P. Visconti, and D. R. Lovley. Fluorescent properties of c-type cytochromes reveal their potential role as an extracytoplasmic electron sink in Geobacter sulfurreducens. *Environmental Microbiology*, 10(2):497–505, 2008.

[25] Y. Fan, E. Sharbrough, and H. Liu. Quantification of the internal resistance distribution of microbial fuel cells. *Environmental Science and Technology*, 42(21):8101–8107, 2008.

[26] A. E. Franks and K. P. Nevin. Microbial Fuel Cells, A Current Review. *Energies*, 3(5):899–919, 2010.

[27] G. Fuhr, R. Hagedorn, T. Muller, W. Benecke, B. Wagner, and J. Gimsa. Asynchronous traveling-wave induced linear motion of living cells. *Studia Biophysica*, 140(2):79–102, 1991.

[28] R. C. Gallo-Villanueva, N. M. Jesús-Pérez, J. I. Martínez-López, A. Pacheco, and B. H. Lapizco-Encinas. Assessment of microalgae viability employing insulator-based dielectrophoresis. *Microfluidics and Nanofluidics*, 2011.

[29] Y. A. Gorby, F. Caccavo Jr, and H. Bolton Jr. Microbial reduction of cobalt(III)EDTA(-) in the presence and absence of manganese(IV) oxide. *Environmental Science and Technology*, 32(2):244–250, 1998.

[30] Y. A. Gorby, S. Yanina, J. S. McLean, K. M. Rosso, D. Moyles, A. Dohnalkova, T. J. Beveridge, I. S. Chang, B. H. Kim, K. S. Kim, D. E. Culley, S. B. Reed, M. F. Romine, D. A. Saffarini, E. A. Hill, L. Shi, D. A. Elias, D. W. Kennedy, G. Pinchuk, K. Watanabe, S. I. Ishii, B. E. Logan, K. H. Nealson, and J. K. Fredrickson. Electrically conductive bacterial nanowires produced by Shewanella oneidensis strain MR-1 and other microorganisms. *Proceedings of the National Academy of Sciences of The United States Of America*, 103(30):11358–11363, 2006.

[31] S. Gupta, R. G. Alargova, P. K. Kilpatrick, and O. D. Velev. On-chip dielectrophoretic coassembly of live cells and particles into responsive biomaterials. *Langmuir*, 26(5):3441–3452, 2010.

[32] B. G. Hawkins and B. J. Kirby. Electrothermal flow effects in insulating (electrodeless) dielectrophoresis systems. *Electrophoresis*, 31(22):3622–3633, 2010.

[33] B. G. Hawkins, A. E. Smith, Y. A. Syed, and B. J. Kirby. Continuous-flow particle separation by 3D insulative dielectrophoresis using coherently shaped, dc-biased, ac electric fields. *Analytical Chemistry*, 79(19):7291–7300, 2007.

[34] B. W. Holloway and B. Fargie. Fertility factors and genetic linkage in Pseudomonas aeruginosa. *Journal of Bacteriology*, 80(3):362–368, sep 1960.

[35] D. E. Holmes, S. K. Chaudhuri, K. P. Nevin, T. Mehta, B. A. Methé, A. Liu, J. E. Ward, T. L. Woodard, J. Webster, and D. R. Lovley. Microarray and genetic analysis of electron transfer to electrodes in Geobacter sulfurreducens. *Environmental Microbiology*, 8(10):1805–1815, 2006.

[36] Y. Huang, R. Hölzel, R. Pethig, and X.-B. Wang. Differences in the ac electrodynamics of viable and nonviable yeast-cells determined through combined dielectrophoresis and electrorotation studies. *Physics in Medicine and Biology*, 37(7):1499–1517, 1992.

[37] J. Johnson and J. CHEN. Taxonomic Relationships Among Strains of Clostridium-Acetobutylicum and Other Phenotypically Similar Organisms. *FEMS Microbiology Reviews*, 17(3):233–240, 1995.

[38] T. B. Jones. *Electromechanics of Particles.* Cambridge University Press, 1995.

[39] T. Kakutani, S. Shibatani, and M. Sugai. Electrorotation of nonspherical cells - theory for ellipsoidal cells with an arbitrary number of shells. *Bioelectrochemistry and Bioenergetics*, 31(2):131–145, 1993.

[40] K. V. Kaler, J. P. Xie, T. B. Jones, and R. Paul. Dual-frequency dielectrophoretic levitation of Canola protoplasts. *Biophysical Journal*, 63(1):58–69, 1992.

[41] B. H. Kim, H. J. Kim, M. S. Hyun, and D. H. Park. Direct electrode reaction of Fe(III)-reducing bacterium, Shewanella putrefaciens. *Journal of Microbiology and Biotechnology*, 9(2):127–131, 1999.

[42] H. J. Kim, M. S. Hyun, I. S. Chang, and B. H. Kim. A microbial fuel cell type lactate biosensor using a metal-reducing bacterium, Shewanella putrefaciens. *Journal of Microbiology and Biotechnology*, 9(3):365–367, 1999.

[43] H. J. Kim, H. Park, M. S. Hyun, I. S. Chang, M. Kim, and B. H. Kim. A mediator-less microbial fuel cell using a metal reducing bacterium, Shewanella putrefaciense. *Enzyme and Microbial Technology*, 30(2):145–152, 2002.

[44] B. Lapizco-Encinas, B. Simmons, E. B. Cummings, and Y. Fintschenko. Dielectrophoretic concentration and separation of live and dead bacteria in an array of insulators. *Analytical Chemistry*, 76(6):1571–1579, 2004.

[45] B. H. Lapizco-Encinas, B. A. Simmons, E. B. Cummings, and Y. Fintschenko. Insulator-based dielectrophoresis for the selective concentration and separation of live bacteria in water. *Electrophoresis*, 25(10-11):1695–1704, 2004.

[46] H. Liu, S. Cheng, and B. E. Logan. Power generation in fed-batch microbial fuel cells as a function of ionic strength, temperature, and reactor configuration. *Environmental Science and Technology*, 39(14):5488–5493, 2005.

[47] H. Liu and B. E. Logan. Electricity generation using an air-cathode single chamber microbial fuel cell in the presence and absence of a proton exchange membrane. *Environmental Science and Technology*, 38(14):4040–4046, 2004.

[48] J. R. Lloyd and L. E. Macaskie. A Novel PhosphorImager-Based Technique for Monitoring the Microbial Reduction of Technetium. *Applied and Environmental Microbiology*, 62(2):578–582, 1996.

[49] B. E. Logan. Exoelectrogenic bacteria that power microbial fuel cells. *Nature Reviews Microbiology*, 7(5):375–381, 2009.

[50] B. E. Logan. Scaling up microbial fuel cells and other bioelectrochemical systems. *Applied Microbiology and Biotechnology*, 85(6):1665–1671, 2010.

[51] D. J. Lonergan, H. L. Jenter, J. D. Coates, E. J. P. Phillips, T. M. Schmidt, and D. R. Lovley. Phylogenetic analysis of dissimilatory Fe(III)-reducing bacteria. *Journal of Bacteriology*, 178(8):2402–2408, 1996.

[52] D. R. Lovley. Microbial fuel cells: novel microbial physiologies and engineering approaches. *Current Opinion in Biotechnology*, 17(3):327–332, 2006.

[53] D. R. Lovley, J. D. Coates, E. L. Blunt-Harris, E. J. P. Phillips, and J. Woodward. Humic substances as electron acceptors for microbial respiration. *Nature*, 382(6590):445–448, 1996.

[54] D. R. Lovley and E. J. P. Phillips. Organic Matter Mineralization with Reduction of Ferric Iron in Anaerobic Sediments. *Applied and Environmental Microbiology*, 51(4):683–689, 1986.

[55] D. R. Lovley and E. J. P. Phillips. Novel Mode of Microbial Energy Metabolism: Organic Carbon Oxidation Coupled to Dissimilatory Reduction of Iron or Manganese. *Applied and Environmental Microbiology*, 54(6):1472–1480, 1988.

[56] D. R. Lovley and E. J. P. Phillips. Reduction of chromate by Desulfovibrio vulgaris and its c(3) cytochrome. *Applied and Environmental Microbiology*, 60(2):726–728, 1994.

[57] D. R. Lovley, E. J. P. Phillips, Y. A. Gorby, and E. R. Landa. Microbial reduction of uranium. *Nature*, 350(6317):413–416, 1991.

[58] D. R. Lovley, P. K. Widman, J. C. Woodward, and E. J. P. Phillips. Reduction of uranium by cytochrome c3 of Desulfovibrio vulgaris. *Applied and Environmental Microbiology*, 59(11):3572–3576, 1993.

[59] M. T. Madigan, J. M. Martinko, P. V. Dunlap, and D. P. Clark. *Brock Biology of Microorganisms*. Pearson/Benjamin Cummings, San Francisco, CA, 12 edition, 2009.

[60] G. H. Markx, Y. Huang, X.-F. Zhou, and R. Pethig. Dielectrophoretic characterization and separation of microorganisms. *Microbiology*, 140:585–591, 1994.

[61] S. Masuda, M. Washizu, and T. Nanba. Novel method of cell-fusion in field constriction area in fluid integrated-circuit. *IEEE Transactions on Industry Applications*, 25(4):732–737, 1989.

[62] T. Mehta, M. V. Coppi, S. E. Childers, and D. R. Lovley. Outer membrane c-type cytochromes required for Fe(III) and Mn(IV) oxide reduction in Geobacter sulfurreducens. *Applied and Environmental Microbiology*, 71(12):8634–8641, 2005.

[63] H. Moncada-Hernández and B. H. Lapizco-Encinas. Simultaneous concentration and separation of microorganisms: insulator-based dielectrophoretic approach. *Analytical and Bioanalytical Chemistry*, 396(5):1805–1816, 2010.

[64] H. Morgan and N. G. Green. Dielectrophoretic manipulation of rod-shaped viral particles. *Journal of Electrostatics*, 42(3):279–293, 1997.

[65] C. R. Myers and K. H. Nealson. Bacterial manganese reduction and growth with manganese oxide as the sole electron acceptor. *Science*, 240(4857):1319–1321, 1988.

[66] K. H. Nealson and D. A. Saffarini. Iron and manganese in anaerobic respiration: environmental significance, physiology, and regulation. *Annual Review of Microbiology*, 48:311–343, 1994.

[67] K. P. Nevin, B.-C. Kim, R. H. Glaven, J. P. Johnson, T. L. Woodard, B. A. Methe, R. J. DiDonato, S. F. Covalla, A. E. Franks, A. Liu, and D. R. Lovley. Anode Biofilm Transcriptomics Reveals Outer Surface Components Essential for High Density Current Production in Geobacter sulfurreducens Fuel Cells. *PLoS One*, 4(5):5628, 2009.

[68] K. P. Nevin and D. R. Lovley. Lack of production of electron-shuttling compounds or solubilization of Fe(III) during reduction of insoluble Fe(III) oxide by Geobacter metallireducens. *Applied and Environmental Microbiology*, 66(5):2248–2251, 2000.

[69] K. P. Nevin, H. Richter, S. F. Covalla, J. P. Johnson, T. L. Woodard, A. L. Orloff, H. Jia, M. Zhang, and D. R. Lovley. Power output and columbic efficiencies from biofilms of Geobacter sulfurreducens comparable to mixed community microbial fuel cells. *Environmental Microbiology*, 10(10):2505–2514, 2008.

[70] T. Niknam, H. Z. Meymand, and M. Nayeripour. A practical algorithm for optimal operation management of distribution network including fuel cell power plants. *Renewable Energy*, 35(8):1696–1714, 2010.

[71] A. Persat, M. E. Suss, and J. G. Santiago. Basic principles of electrolyte chemistry for microfluidic electrokinetics. Part II: Coupling between ion mobility, electrolysis, and acid-base equilibria. *Lab on a Chip*, 9(17):2454–2469, 2009.

[72] R. Pethig. Review Article-Dielectrophoresis: Status of the theory, technology, and applications. *Biomicrofluidics*, 4(2):022811–022811, 2010.

[73] H. A. Pohl. The motion and precipitation of suspensoids in divergent electric fields. *Journal of Applied Physics*, 22(7):869–871, 1951.

[74] H. A. Pohl. *Dielectrophoresis.* Cambridge University Press, 1978.

[75] M. Potter. Electrical effects accompanying the decomposition of organic compounds. *Proceedings of the Royal Society of London: Series B*, 84(571):260–276, 1911.

[76] J. A. Price, J. P. Burt, and R. Pethig. Applications of a new optical technique for measuring the dielectrophoretic behaviour of micro-organisms. *Biochimica et Biophysica Acta*, 964(2):221–230, 1988.

[77] M. D. Pysher and M. A. Hayes. Electrophoretic and dielectrophoretic field gradient technique for separating bioparticles. *Analytical Chemistry*, 79(12):4552–4557, 2007.

[78] F. Qian, M. Baum, Q. Gu, and D. E. Morse. A 1.5 microL microbial fuel cell for on-chip bioelectricity generation. *Lab on a Chip*, 9(21):3076–3081, 2009.

[79] K. Rabaey, N. Boon, S. D. Siciliano, M. Verhaege, and W. Verstraete. Biofuel cells select for microbial consortia that self-mediate electron transfer. *Applied and Environmental Microbiology*, 70(9):5373–5382, 2004.

[80] G. Reguera, K. D. McCarthy, T. Mehta, J. S. Nicoll, M. T. Tuominen, and D. R. Lovley. Extracellular electron transfer via microbial nanowires. *Nature*, 435(7045):1098–1101, 2005.

[81] G. Reguera, K. P. Nevin, J. S. Nicoll, S. F. Covalla, T. L. Woodard, and D. R. Lovley. Biofilm and nanowire production leads to increased current in Geobacter sulfurreducens fuel cells. *Applied and Environmental Microbiology*, 72(11):7345–7348, 2006.

[82] H. Richter, K. P. Nevin, H. Jia, D. A. Lowy, D. R. Lovley, and L. M. Tender. Cyclic voltammetry of biofilms of wild type and mutant Geobacter sulfurreducens on fuel cell anodes indicates possible roles of OmcB, OmcZ, type IV pili, and protons in extracellular electron transfer. *Energy and Environmental Science*, 2(5):506–516, 2009.

[83] B. R. Ringeisen, E. Henderson, P. K. Wu, J. Pietron, R. Ray, B. Little, J. C. Biffinger, and J. M. Jones-Meehan. High power density from a miniature microbial fuel cell using Shewanella oneidensis DSP10. *Environmental Science and Technology*, 40(8):2629–2634, 2006.

[84] E. E. Roden and D. R. Lovley. Dissimilatory Fe(III) Reduction by the Marine Microorganism Desulfuromonas acetoxidans. *Applied and Environmental Microbiology*, 59(3):734–742, 1993.

[85] E. E. Roden and J. M. Zachara. Microbial reduction of crystalline iron(III) oxides: Influence of oxide surface area and potential for cell growth. *Environmental Science and Technology*, 30(5):1618–1628, 1996.

[86] R. Rusconi, S. Lecuyer, L. Guglielmini, and H. A. Stone. Laminar flow around corners triggers the formation of biofilm streamers. *Journal of the Royal Society Interface*, 7(50):1293–1299, 2010.

[87] D. T. Scott, D. M. McKnight, E. L. Blunt-Harris, S. E. Kolesar, and D. R. Lovley. Quinone moieties act as electron acceptors in the reduction of humic substances by humics-reducing microorganisms. *Environmental Science and Technology*, 32(19):2984–2989, 1998.

[88] T. Sharma, A. L. M. Reddy, T. S. Chandra, and S. Ramaprabhu. Development of carbon nanotubes and nanofluids based microbial fuel cell. *International Journal of Hydrogen Energy*, 33(22):6749–6754, 2008.

[89] Y.-Y. Shi. Low reynolds numbers flow past an ellipsoid of revolution of large aspect ratio. *Journal of Fluid Mechanics*, 23:657–671, 1965.

[90] A. Shukla, P. Suresh, S. Berchmans, and A. Rajendran. Biological fuel cells and their applications. *Current Science*, 87(4):455–468, 2004.

[91] P. Smid. *CNC programming handbook.* Industrial Press Inc., New York, NY, 2003.

[92] B. Soni, P. Soucaille, and G. Goma. Continuous Acetone-Butanol Fermentation - a Global Approach for the Improvement in the Solvent Productivity in Synthetic Medium. *Applied Microbiology and Biotechnology*, 25(4):317–321, 1987.

[93] W. STAMM. Catheter-Associated Urinary-Tract Infections - Epidemiology, Pathogenesis, and Prevention. *American Journal of Medicine*, 91:S65–S71, 1991.

[94] S. J. R. Staton, K. P. Chen, T. J. Taylor, J. R. Pacheco, and M. A. Hayes. Characterization of particle capture in a sawtooth patterned insulating electrokinetic microfluidic device. *Electrophoresis*, 31(22):3634–3641, 2010.

[95] N. Swami, C.-F. Chou, V. Ramamurthy, and V. Chaurey. Enhancing DNA hybridization kinetics through constriction-based dielectrophoresis. *Lab on a Chip*, 9(22):3212–3220, 2009.

[96] R. M. Vejborg, V. Hancock, M. A. Schembri, and P. Klemm. Comparative Genomics of Urinary Tract Infectious Escherichia coli. *Applied and Environmental Microbiology*, 2011. in press.

[97] K. Venkateswaran, D. P. Moser, M. E. Dollhopf, D. P. Lies, D. A. Saffarini, B. J. MacGregor, D. B. Ringelberg, D. C. White, M. Nishijima, H. Sano, J. Burghardt, E. Stackebrandt, and K. H. Nealson. Polyphasic taxonomy of the genus Shewanella and description of Shewanella oneidensis sp. nov. *International Journal of Systematic Bacteriology*, 49(2):705, 1999.

[98] H. von Canstein, J. Ogawa, S. Shimizu, and J. R. Lloyd. Secretion of flavins by Shewanella species and their role in extracellular electron transfer. *Applied and Environmental Microbiology*, 74(3):615–623, 2008.

[99] M. Washizu, S. Suzuki, O. Kurosawa, T. Nishizaka, and T. Shinohara. Molecular dielectrophoresis of biopolymers. *IEEE Transactions On Industry Applications*, 30(4):835–843, 1994.

[100] J. J. Weigle and M. Delbrück. Mutual exclusion between an infecting phage and a carried phage. *Journal of Bacteriology*, 62(3):301, 1951.

[101] K. Wildes and N. Lindgren. *A century of electrical engineering and computer science at MIT.* MIT Press, Cambridge, MA, 1985.

[102] R. E. Wildung, Y. A. Gorby, K. M. Krupka, N. J. Hess, S. W. Li, A. E. Plymale, J. P. McKinley, and J. K. Fredrickson. Effect of electron donor and solution chemistry on products of dissimilatory reduction of technetium by Shewanella putrefaciens. *Applied and Environmental Microbiology*, 66(6):2451–2460, 2000.

[103] Y. Xia and G. M. Whitesides. Soft lithography. *Angewandte Chemie International Edition*, 37:550–575, 1998.

[104] F. Zhang, K. S. Jacobson, P. Torres, and Z. He. Effects of anolyte recirculation rates and catholytes on electricity generation in a litre-scale upflow microbial fuel cell. *Energy and Environmental Science*, 3:1347–1352, 2010.

[105] J. Zhu and X. Xuan. Dielectrophoretic focusing of particles in a microchannel constriction using DC-biased AC flectric fields. *Electrophoresis*, 30(15):2668–2675, 2009.